European Journal of Mechanics B/Fluids 28 (2009) 444–464

Contents lists available at ScienceDirect

European Journal of Mechanics B/Fluids

www.elsevier.com/locate/ejmflu

Experiments and modeling of cavitating flows in venturi: attached sheet cavitation

S. Barre *, J. Rolland, G. Boitel, E. Goncalves, R. Fortes Patella

Laboratoire des Ecoulements Géophysiques et Industriels (LEGI – CNRS – INPG – UJF), BP53, 38041 Grenoble, France

ARTICLE INFO

Article history:
Received 5 July 2007
Received in revised form 28 April 2008
Accepted 4 September 2008
Available online 13 September 2008

Keywords:
Cavitation
Modeling
Optical probe
Two-phase flow

ABSTRACT

Correlated experimental and numerical studies were carried out to analyze cavitating flows and to describe the two-phase flow structures of attached sheet cavitation in Venturi geometries. New double optical probe measurements were performed and special data processing methods were developed to estimate void ratio and velocity fields for cold water flows.

By applying a computational method previously developed in LEGI (*Laboratoire des Ecoulements Géophysiques et Industriels, Grenoble, France*) based on the code Fine^{TM}/Turbo and on a barotropic approach, several steady calculations were performed in cold water cavitating flows. Local and global analyzes based on comparisons between experimental and numerical results were proposed.

0. Introduction

The present work follows previous experimental and numerical studies carried out by the Turbomachinery and Cavitation team of LEGI (*Laboratoire des Ecoulements Géophysiques et Industriels, Grenoble, France*) (Stutz and Reboud [1–4]; Pouffary et al. [5,6]; Coutier-Delgosha et al. [7]).

The main purpose of this paper is to describe the two-phase flow structure of a "quasi-stable" attached cavitation sheet both by experiments and computational fluid dynamics (CFD) means. An accurate description of the two-phase structure is essential to describe the cavitation process occurring in this kind of flow. Furthermore, confrontation between experimental and CFD results are essential to validate and to improve physical and numerical cavitating flow models.

Because of cavitating flow complexity, the main challenges are to obtain experimentally void ratio and velocity fields inside the sheet, and to perform reliable numerical simulations.

Experimental studies in cavitation sheets were often limited to the measurements of global flow characteristics or eventually to some local data in the surrounding liquid flow area. Previous work mainly focused on pressure and temperature fields at the wall, external flow velocity and geometrical description of the cavity shapes. See for example Laberteaux et al. [8], Le et al. [9] and Callenaere et al. [10] among others. On the opposite, the two-phase flow structure of attached cavities has been the subject of very few measurements. Let us recall the work of Kamono et al. [11] who performed velocity measurements in natural and ventilated cavities using a double hot-wire anemometer on a foil section. Bubble detection was also performed by Ceccio and Brennen [12] who used silver epoxy electrodes flush-mounted on a hydrofoil surface for individual bubble velocity detection.

More recently some other techniques have been applied to the investigation of such diphasic flows. Iyer and Ceccio [13] used Fluorescent Particle Image Velocimetry (PIV-LIF) to obtain both the mean velocity field and the Reynolds stress tensor in a cavitating turbulent free shear layer. Dular et al. [14] also used PIV-LIF technique to obtain the velocity field inside and outside of the cavitation sheet existing on a hydrofoil model. It is clear that PIV-LIF is a particularly performing tool to obtain mean and turbulent velocity fields. However it is a very expensive and sophisticated technique and it is almost impossible to perform precise local void ratio measurements with such technology. It must then be coupled to another measurement system to obtain this information in the studied flow.

This can be done by using X-ray absorption technique which is a very performing tool to measure void ratio in two-phase cavitating flows. Using this system we can obtain a very reliable estimation of the void ratio field. This technique may be used with two kinds of data processing methods:

- Firstly, acquisition of spatially integrated void ratio temporal variations. This process was used by Stutz et al. [15] to qualify the dynamic behavior of a cavitation sheet over a Venturi with strong adverse pressure gradient leading to a periodic pulsation of the rear part of the sheet.
- Secondly, acquisition of the spatial distribution of temporally averaged void ratio by a tomographic reconstruction algorithm of the void ratio field. Results on a very complex 3D geometry (Rocket turbopump inducer) were obtained in our team by Hassan et al. [16,17]. They described the spatial and temporal

* Corresponding author.
E-mail address: stephane.barre@hmg.inpg.fr (S. Barre).

0997-7546/$ – see front matter
doi:10.1016/j.euromechflu.2008.09.001

repartition of the void ratio over the entire flow field in a real rocket engine turbopump inducer.

However the X-Ray absorption technique is not able to measure exactly the mean and turbulent velocity fields at a sufficiently fine spatial resolution to obtain mean and fluctuating values compatibles with Reynolds averaging hypothesis.

It is clear that both the PIV-LIF and X-ray absorption techniques are presumably one of the best possible choices available today to obtain velocity and/or void-ratio fields in cavitating two-phase flows. The main counterpart is that they are very expensive and that they must be used in a synergy process to obtain data both on velocity and void ratio fields. On the opposite, the use of double optical probe is a very cheap method to obtain, from only one measurement, rather accurate data about both velocity and void ratio fields. We then decide, in the present work, to use a double optical probe (as in Stutz and Reboud [2] and Stutz [4]) to perform both void ratio and longitudinal velocity measurements. This technique has been chosen among other possibilities (see Stutz and Reboud [1] for a review) because it has proven to be well adapted to the particular flow configuration under study.

The present work is an extension of Stutz's one [4]. The experimental technique has been improved and particularly, a new algorithm has been introduced to perform velocity-field statistic computations. Furthermore, comparisons with CFD results have been done to assess and calibrate numerical tools developed in our team and applied to simulate 2D and 3D cavitating flows (Pouffary et al. [5,6,18], Coutier-Delgosha et al. [7]).

The studies fit into a research logic carried out for many years by our team in collaboration with the French Space Agency (*Centre National d'Etudes Spatiales, CNES*) and the Rocket Engine Division of Snecma. The aims are to develop, to calibrate, to validate modeling tools in order to simulate the cavitating operation of rocket engine turbopump inducers, and to progress in the understanding and prediction of the mechanisms associated with cavitation in the case of cryogenic fluids, like LH2 and LOx.

In this context, in a parallel with experimental studies, two simulation tools using different numerical schemes have been developed, based mainly on the barotropic cavitation model proposed by Delannoy and Kueny [19], which links the fluid density to the pressure variations. The first numerical code, named "IZ", allows 2D simulations and has been widely applied in our team to analyze unsteady cavitating flows (Reboud et al. [20]; Lohrberg et al. [21]; Coutier-Delgosha et al. [22,23], Fortes et al. [24]). More recently, through collaborations between the LEGI laboratory and Numeca International, the cavitation physical model was implemented in the commercial code Fine/Turbo^{TM}, which allows 3D simulations in turbomachinery geometries (Pouffary et al. [5], Coutier-Delgosha et al. [7]). Previous versions of this numerical tool have been applied and tested also on various 2D flow configurations (Pouffary et al. [6,18]).

On steady configurations, the calibration and validation of the code have been performed considering global flow parameters, such as, for example, cavity length, total vapor volume and global machinery performances (Pouffary et al. [5], Coutier-Delgosha et al. [7,25]). Unsteady calculations performed with this code have provided very good qualitative results and analyzes (Pouffary et al. [6,18]), but no quantitative validation has been carried out in these cases.

In spite of the progress of CFD, unsteady calculations, mainly in turbomachinery geometries, are very time consuming and a steady approach is still interesting (even if it cannot represent the physical mechanisms observed completely). In this context, in complement to previous works and in order to carry on with calibration/validation of Fine/Turbo^{TM}, calculations performed in the present study aim to evaluate the capability of the numerical tool to predict local parameters of cavitating flows (void ratio, pressure and velocity fields) from a steady approach.

As a step to develop and test numerical and experimental tools, in this paper we present studies performed in the case of cold water. In order to facilitate and to carry out local measurements and analyzes, cavitating flows inside space turbopump inducers are simulated by Venturi geometries.

Section 1 presents the experimental device used for recent tests in cold water. Section 2 describes the new data processing methods developed to evaluate, from measurements by double optical probes, the void ratio and velocity fields in cavitating flows. The experimental approach has been applied for a Venturi geometry (named "Venturi 4°"), where the cavitating flow is characterized by a quasi-steady attached sheet cavitation. Comparisons with previous experimental results obtained by Stutz [4] are presented in Section 3.

The numerical model applied to simulate water cavitating flow in "Venturi 4°" geometry is presented in Section 4. Global and local analyzes based on the comparison between experimental and numerical results are presented in Section 5.

1. Experimental device

The experimental device includes mainly a test loop and a sensor (a double optical probe) associated with an acquisition module.

1.1. The test loop

The Venturi type test section of the CREMHYG (INPG Grenoble) cavitation small tunnel was dimensioned and designed to simulate cavitating flows developing on the blades of space turbopump inducers. The hydraulic system (Fig. 1) is composed of a circulation pump and of a free surface tank, used to impose the reference pressure in the circuit and to resorb dissolved gases. The flow rate, controlled by a computer, is measured by means of an electromagnetic flow meter. The pressure within the flow is measured by two sensors located in the free surface tank and in the entry section of the Venturi (S_i). The adjustment of the pressure in the circuit is obtained by managing the air pressure over the free surface of the tank by means of a vacuum pump. The measurement accuracies are evaluated to be:

$$\Delta Q/Q = \pm 0{,}25\% \quad \text{for flow rate,}$$

$$\Delta P = \pm 0{,}05 \text{ bar} \quad \text{for the pressure.}$$

The Venturi test section consists in parallel sidewalls generating rectangular cross sections. The bottom wall can be equipped with several interchangeable Venturi profiles allowing the study of cavitation on various geometries. These profiles are equipped to receive pressure sensors, temperature sensors, or double optical probes.

In the present study, we use a profile with a convergence angle of 4.3° and a divergence angle of 4°, illustrated in Fig. 2. The edge forming the throat of the Venturi is used to fix the separation point of the cavitation cavity. This profile is characterized by the following geometrical data:

Inlet section: $S_i = 50 \times 44$ mm^2 (where the reference pressure is measured);
Throat section: $S_{\text{throat}} = 43.7 \times 44$ mm^2;
Length of the test section (chord): $L_{\text{ref}} = 252$ mm.

This profile is equipped with five probing holes to take various measurements such as the local void ratio, instantaneous local speed and pressure. Their horizontal positions X_I from the throat of the Venturi are:

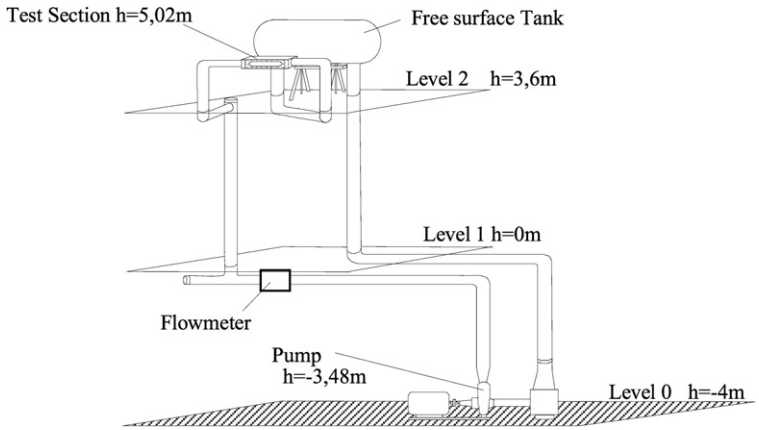

Fig. 1. Schematic view of the hydraulic set-up.

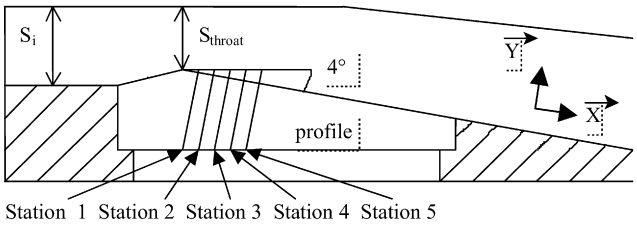

Fig. 2. Schematic view of the Venturi profile.

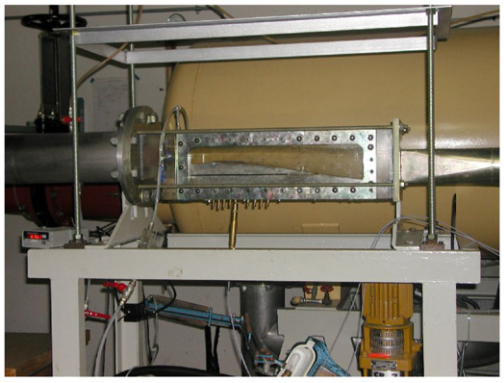

Fig. 3. Venturi test section.

$X_1 = 5.1$ mm; $X_2 = 20.9$ mm; $X_3 = 38.4$ mm;

$X_4 = 55.8$ mm; $X_5 = 73.9$ mm.

A photograph of this test section is shown in Fig. 3.

The selected operation point of the hydraulic system is the same used by Stutz et al. [1,4]. It is characterized by the following physical parameters:

$U_{\text{inlet}} = 10.8$ m/s: inlet speed
$Q = 0.02375$ m^3/s: flow imposed in the circuit by the circulating pump
$P_{\text{tank}} = 0.713$ bar: pressure measured in the tank
$P_{\text{inlet}} = 36\,000$ Pa: pressure in the inlet section
$N_{\text{pump}} = 506$ rpm: rotating speed of the circulating pump.

With these parameters, we obtain a cavity length L ranging between 70 mm $\leqslant L \leqslant$ 85 mm, and having a relatively stable aspect, as shown on Fig. 4.

1.2. The sensor

To evaluate void ratio and velocity fields inside the cavity, we have used a double optical probe. The double optical probe is an intrusive sensor composed by two mono-probes functioning in a independent way but mechanically connected one to other. Each probe consists in an optical fiber ending in a frayed Sapphire point. This point is plunged in the flow. An infra-red radiation is injected at an end of the fiber. The part of this signal that is reflected at the tip of the probe is converted into electric signal by an opto-electronic module.

The luminous ray is absorbed by the fluid when the tip of the probe is surrounded by liquid; in this case, the measured tension is minimal. When the tip is in a pure vapor zone, the measured tension is maximal. The signal analysis enables the determination of the phase (liquid or gas) of the flow structures around the probe. This information gives access to the local time fraction of the vapor phase (void rate) and the convection speed of the vapor structures. We use an optical probe made of two optical fibers of 80 μm diameter with frayed ends. The inter-tip distance is 1.05 mm $\pm$ 0.02 (see Fig. 5).

The double probe is introduced into the cavitation sheet using a threaded interface assembled in the boreholes of the profile (also called “stations”). A graduated sliding gauge enables the measurement of the vertical displacement of the probe with an accuracy of $\Delta Y = \pm 0.05$ mm. The optical signals obtained by the double probe are transformed into electric signals by an optoelectronic module. The values of the gains and the zeros of the apparatus are tuned in order to obtain exit signals of ± 1 V amplitude. Acquisitions are carried out on a fast A/D data acquisition board NI-DAQ PCI-6110E and a microcomputer. For each acquisition we recorded 6 million points per way (one way by optical probe), with a sampling rate of 100 KHz (corresponding to a time of 60 seconds acquisition per measurement). For each Y position of the optical probe in the Venturi (between ten and fifteen per station), five successive measurements are taken. It generates 30 million points of measurement per position in the cavity corresponding to an observation time of 300 s. This new experimental tool increases clearly the overall performance of the entire system as compared to the work performed by Stutz in the same device (Stutz [4]). The main differences are:

– At first, the double optical probe was changed by decreasing the distance Δx between the two probes. We now use a $\Delta x = 1.05$ mm instead of 2.02 mm in Stutz’s experiments. The probe design is also new. In the present study, we use Sapphire tips probes instead of silica ones. The main advantage of such a technology lies in a better robustness of the probe

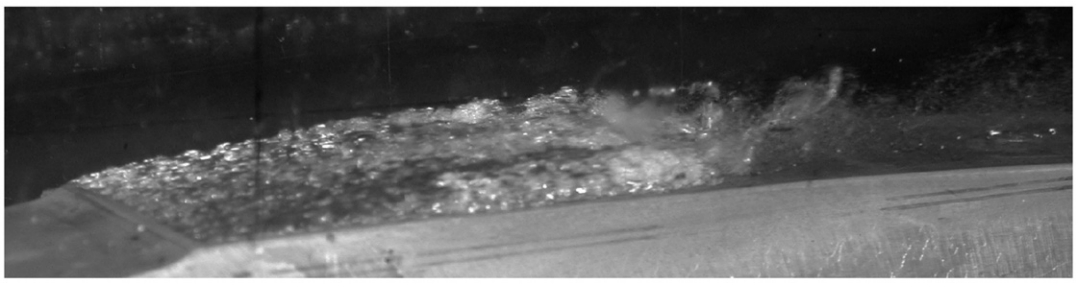

Fig. 4. Photograph of the cavity.

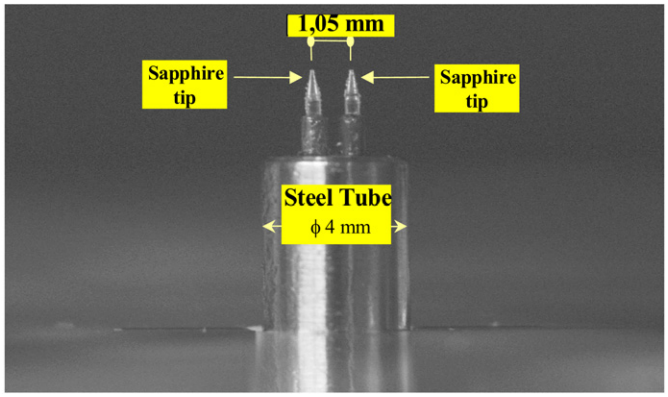

Fig. 5. Double optical probe.

tips avoiding probe breaks when used in very aggressive flows such as re-entrant jets at the bottom of the cavitation sheet:

- The optoelectronics module used in the present experiment remains the same as the one used in Stutz's experiments (Stutz [4]). It has a response time of 1 µs.
- We can also notice that the observation time was of 9 s for each measurement in Stutz [4] instead of 300 s in the present study. This great increase may lead us to obtain rather better statistical results: in particular, the Velocity Probability Density Functions (PDF) is much more accurately defined.
- The data processing method developed to obtain velocity PDF is based on the concept presented by Stutz [4] but was greatly modified to increase the quality of the PDF computation, as described in the next section.

1.3. Wall pressure measurement device

In the context of the present experimental study, the mean wall pressures were also measured for nine probed stations including the five stations inside the cavitation sheet (where void ratio and velocity measurements were performed) and also four other stations placed downstream in the wake of the sheet in order to describe the pressure recovery process after the cavitating zone. The sensor was an absolute one. We use a piezoelectric sensor DRUCK model N° PMP4070 with a maximum range of 70 000 Pa. Its relative precision is ±0.027% giving then an absolute precision of ±19 Pa.

The corresponding results are presented together with numerical predictions ones in Section 5.3.4 of the present paper.

2. Data processing methods

2.1. Estimation of the local void ratio

The local void ratio α of a vapor/liquid mixture is defined here as the ratio between the cumulated attendance time of the vapor phase $\sum_{i=1}^{n} T_{\text{vap\_}i}$ and a given time of observation $T_{\text{tot\_obs}}$ in an operation point of the flow. It is given by:

$$\alpha = \frac{\sum_{i=1}^{n} T_{\text{vap\_}i}}{T_{\text{tot\_obs}}}.$$

The post processing algorithm enables us to process the signal from the optical probe, by distinguishing the vapor phase from the liquid phase according to the value of the measured tension. The maximum tension value $V_{\max}$ corresponds to the vapor phase and the minimal value $V_{\min}$ to the liquid phase (Fig. 6). In order to be able to estimate the local void ratio, we must fix a threshold tension: $V_{\text{threshold}}$. It makes it possible to determine the phase of the fluid around the probe: liquid state if $V < V_{\text{threshold}}$ and vapor state if $V > V_{\text{threshold}}$. This threshold is fixed, in this study, according to the parameter:

$$\beta = \frac{V_{\text{threshold}} - V_{\min}}{V_{\max} - V_{\min}}.$$

The value of this parameter for this kind of flow was gauged by Stutz et al. [1–4,26] using a γ Ray absorption device. They retained a value of $\beta = 0.1$ to give correct void ratios for this typical flow pattern. In the present work, we have used this value for the determination of the void ratio.

With all this experimental procedure the relative uncertainty on the void ratio measurement was estimated to about 15% by Stutz [4] and we may admit this value for the present study.

2.2. Estimation of instantaneous local velocity

The basic idea used to determine the instantaneous velocities in two-phase flows was firstly developed by Serisawa et al. [27] and Revankar and Ishii [28] and applied by Stutz [4] in the case of cavitating flows. The principle is relatively simple and consists in comparing the transit time of two bubbles successively detected by probe 1 (S1) and probe 2 (S2). If these two transit times are sufficiently close together we may then consider that we have observed consecutively the same bubble on S1 and S2. We can then compute the longitudinal velocity component using the time delay between the beginning of the bubble detection on S1 and the same event on S2. In the present study, we have developed a new algorithm to compute the Velocity Probability Density Function (PDF) which is quite different to the one used by Stutz [4]. The new approach is described in detail hereafter.

The used optical probe, aligned in the direction of the flow, produces two distinct signals (S1 upstream and S2 downstream). It is possible to deduce the value of the tangential component (parallel to the profile) of the instantaneous local speed by considering the temporal shift between the trace of a bubble passing on the first probe and that of this same bubble passing on the second probe. For this, it is necessary to detect the vapor bubbles. The electric signals of the two optical probes are thus analyzed and broken up by introducing two tension thresholds (Fig. 7). The low threshold V_{low}, taken on the rising part of the electric signal, leads us to

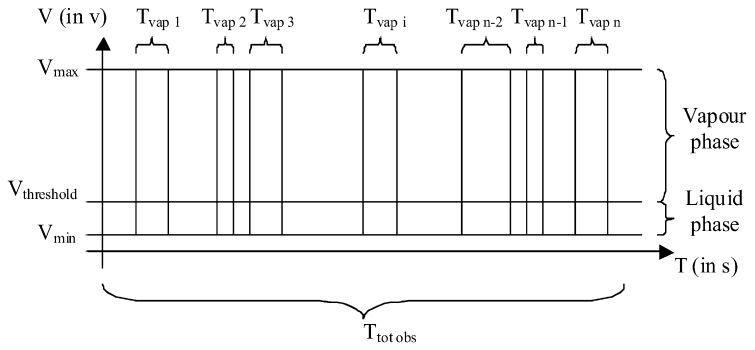

Fig. 6. Relative positions of the thresholds for void ratio analysis.

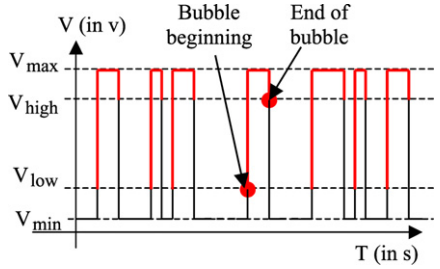

Fig. 7. Bubble localization with threshold method.

detect the beginning of the crossing of a vapor bubble. The high threshold V_{high} is considered to detect the end of the crossing of the bubble on the downward part of the signal. A bubble is taken into account in the analysis only when these two thresholds are crossed consecutively.

In the present study, the values of the low and high thresholds are given by considering the parameters:

$$\beta_{low} = \frac{V_{low} - V_{min}}{V_{max} - V_{min}} \quad \text{and} \quad \beta_{high} = \frac{V_{high} - V_{min}}{V_{max} - V_{min}}$$

where $\beta_{low} = 0.2$ and $\beta_{high} = 0.8$ (Stutz et al. [1,2,4,19]). An analysis of the β value influence on the velocity evaluation has been performed and shows that for β_{low} and β_{high} close to respectively 0.2 and 0.8, variations of the β value of ±15% have only a very weak effect on the velocity determination.

After bubble detection by both probes, we proceed to the evaluation of the instantaneous velocities. The algorithm used to obtain these data, as well as the various statistical treatment procedures applied to evaluate the corresponding Probability Density Functions (PDF) are described hereafter.

First of all, the calculation algorithm reviews all the bubbles detected on probe S1 (first probe in the direction of the flow). For each bubble seen on S1, a temporal analysis interval will be explored on the signal of probe S2.

If *Ideb1* is the index corresponding to the beginning of a bubble considered on the S1 signal, then the analysis interval of the S2 signal will correspond to $Ideb1 - Itau < t < Ideb1 + Itau$, where *Itau* is the amplitude of the analysis interval. Stutz et al. [1,2,19] proposed to determine *Itau* by using the value of the peak of the temporal correlation function between the signals resulting from S1 and S2. In the present study, however, we chose an empirically constant value evaluated from the various examinations obtained. This value is fixed here at $Itau = 1{,}000$, which corresponds to a temporal analysis interval of $\Delta T = \pm Itau \times Tech = \pm 10$ ms, where *Tech* is the sampling period of the optical probe signals ($Tech = 1/Fech = 10^{-5}$ s) and *Fech* is the sampling frequency. With this ΔT range the theoretical corresponding velocity field under examination is: (-105 m/s $< U < -0.105$ m/s) and (0.105 m/s $< U <$ 105 m/s). Absolute value of velocity of 0.105 m/s corresponds to $Itau = 1000$ and the value $U = 105$ m/s corresponds to $Itau = 1$. Thus, we seek all the existing bubbles on the S2 probe signal in the analysis interval defined. For each one of these bubbles, a test function is calculated as follows:

We calculate the parameter $\varepsilon = (t_1 - t_2(i))/t_1$ where t_1 is the transit time of the bubble considered on S1 and $t_2(i)$ the transit times of the bubbles found on S2 in the analysis interval (see Fig. 8 for illustration). From the evaluation of all ε parameters obtained for all the bubbles found on S2 in the research interval ΔT, the minimum value ε_{min} is determined. The bubble corresponding to the value of ε_{min} must now be validated or not according to the value of this test. In this study, the validation criterion corresponds to ε_{min} lower or equal to $\varepsilon_{max} = 0.1$, which was empirically determined by a convergence test and a parametric study of the influence of ε_{max} on the velocity fields obtained.

By applying this criterion, we rejected approximately 60% of the detected bubbles. If the bubble was validated on S2, we computed its temporal shift with the reference bubble of S1. We then obtained $Itauopt = Ideb2 - Ideb1$ where *Ideb1* and *Ideb2* are, respectively, the indices of beginning of bubbles on the signals of both S1 and S2 probes (see Fig. 8 for illustration). From *Itauopt*, we obtain an instantaneous speed value by: $u = \frac{\Delta x}{Itauopt \times Tech}$ where Δx is the space difference between the two optical probes ($\Delta x = 1.05$ mm) and *Tech* is the sampling period of the optical probe signals.

By repeating this operation on all the detected bubbles on the S1 probe, we obtain an instantaneous velocity values population, which can be treated in a statistical way to study the dynamics of the flow. For the present study, we obtain 5 000 to 70 000 values of instantaneous speeds per spatial position of the probes typically, and this, for an observation time of 300 s. It is worth noting that the higher the void ratio is, the higher the number of studied bubbles is and the better the statistic quality is. Following this process we can obtain, for each measurement point in the flow, the *Itauopt* and velocity PDF. An example of a statistical distribution obtained is given on Figs. 9 (*Itauopt*) and 10 (*velocity*). This example corresponds to point $Y = 1$ mm of station N° 2 (Fig. 2).

An important amount of the *Itauopt* population around the peak is noticed, representing the most probable value for the considered measurement point (Fig. 9). Moreover, for high absolute values of *Itauopt*, the populations do not decrease and tend to reach an asymptotic value. From Fig. 10, we can see, near velocity zero value, a regrouping of the occurrences corresponding to the two asymptotic branches of the *Itauopt* distribution. This effect of overpopulation is accentuated by the fact that speed being inversely proportional to *Itauopt*, so all the high values (in absolute value) for *Itauopt* correspond to a very small speed range around zero value. This population corresponds in fact to a statistical bias of the algorithm used to evaluate velocity values.

Indeed, following the algorithm, we seek a bubble on signal S2 whose duration is almost equivalent to the basic bubble located on S1. Then, the probability of finding a solution for the prob-

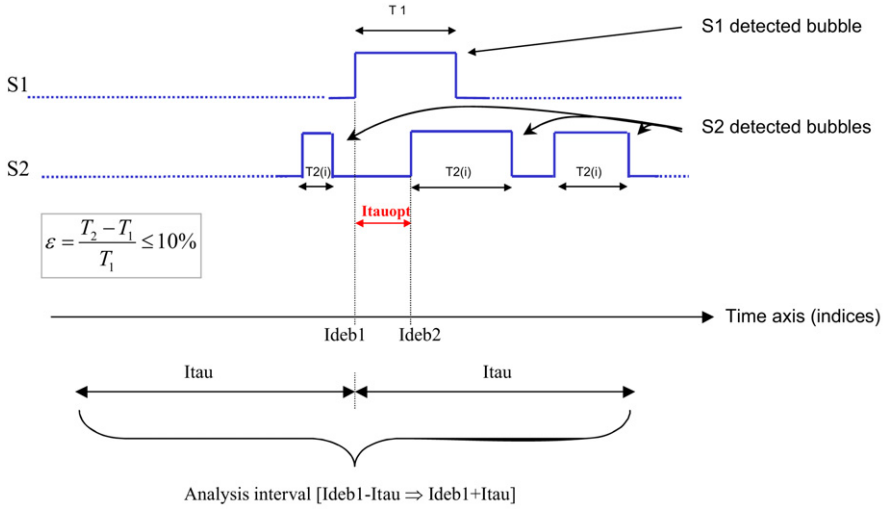

Fig. 8. Example of *Itauopt* determination for a given bubble detected on S1.

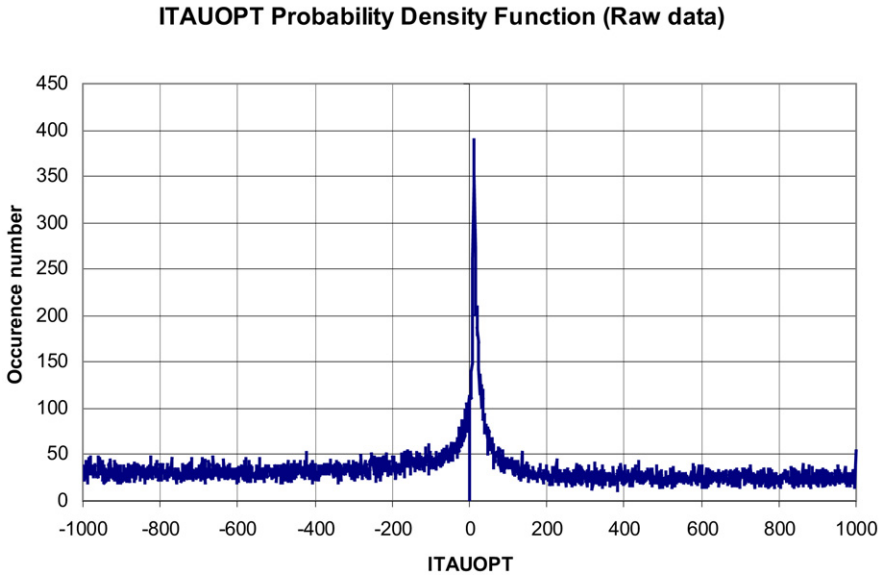

Fig. 9. PDF of *Itauopt* values initially obtained (station 2, $Y = 1$ mm).

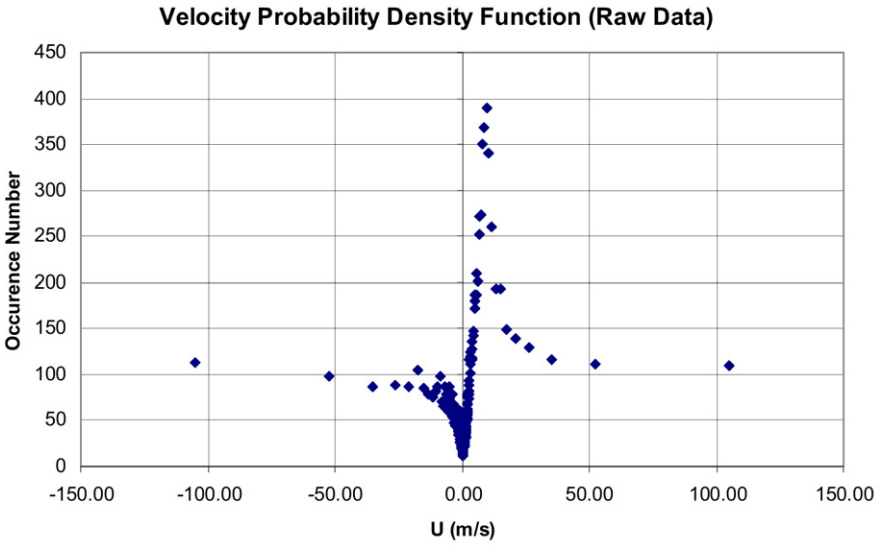

Fig. 10. PDF of velocity values initially evaluated (station 2, $Y = 1$ mm).

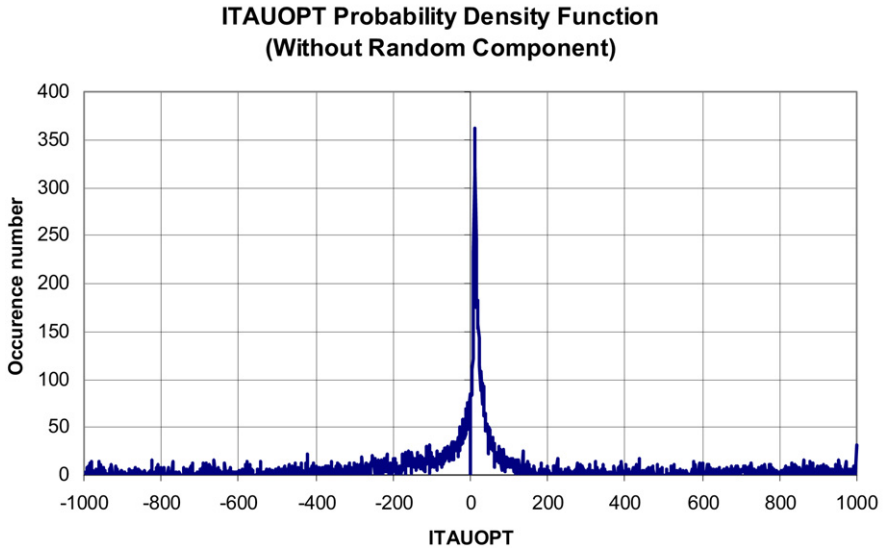

Fig. 11. *Itauopt* PDF obtained by subtraction of random distribution (Poisson law correction).

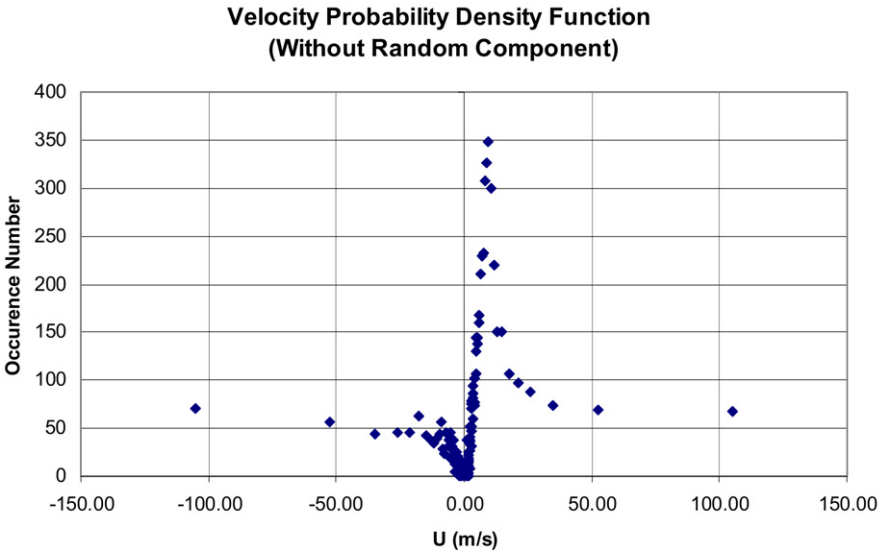

Fig. 12. Velocity PDF obtained by subtraction of random distribution (Poisson law correction).

lem increases with the *Itau* amplitude of the analysis interval. As a matter of fact, if signals from S1 and S2 were perfectly random, the velocity Probability Density Function would be a Poisson law centered around the zero value speed. This law, which is superimposed on the PDF, must be eliminated. Its contribution on the PDF of the real flow can be removed by using a "neutral" *Itauopt* PDF, which considers only "background noise". It is determined thanks to the PDF asymptotic parts. Fig. 11 illustrates an example of the PDF obtained after Poisson law correction.

In spite of this correction, we observe (Fig. 12) numerous populations for relatively high speed absolute values.

This effect is related to the inaccuracy of the method for high speed. Indeed, because *Itauopt* is an integer number, the measurement method does not give infinity of possible values for velocity. The accuracy on the velocity evaluation much depends on the *Itauopt* value. In order to visualize and quantify this effect better, the relative error function $\phi = (U_{Itauopt+1} - U_{Itauopt})/U_{Itauopt}$ was calculated for each value of *Itauopt* in the range corresponding to the considered flow. These results are presented in Fig. 13 where function ϕ is plotted for values of U between 1 and 20 m/s.

The accuracy is about 1% in the region of 1 m/s, but it increases to reach 16% towards 20 m/s. Moreover, we note for $U \geqslant 10$ m/s that the possible speed distribution is represented by few discrete solutions, which are separated each other by several m/s.

We may now obtain the global relative accuracy on velocity determination as follows:

$$\frac{\Delta U}{U} = \frac{\Delta(\Delta x)}{\Delta x} + \frac{\Delta t}{t}$$

where Δx is the probe spacing and t the bubble transit time. Expressing t and Δt from the other data leads to:

$$\frac{\Delta U}{U} = \frac{\Delta(\Delta x)}{\Delta x} + \frac{U}{\Delta x f_{\text{ech}}}$$

where f_{ech} is the sampling frequency. The value of $(\Delta(\Delta x))/\Delta x$ is a constant equal to 1% and the value of $U/(\Delta x f_{\text{ech}})$ is plotted on Fig. 13.

In fact, the velocity solutions are gathered according to these few possible values, which artificially increase their population. To correct this effect, the samples are distributed at high speed in a more continuous way by proceeding to an oversampling of the PDF. Several assumptions are formulated for this purpose:

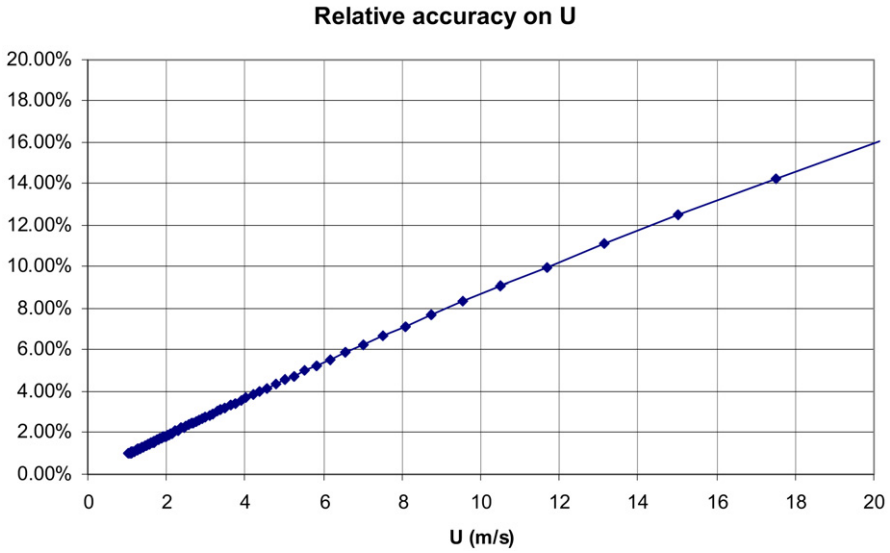

Fig. 13. Relative error function ϕ in the studied velocity range.

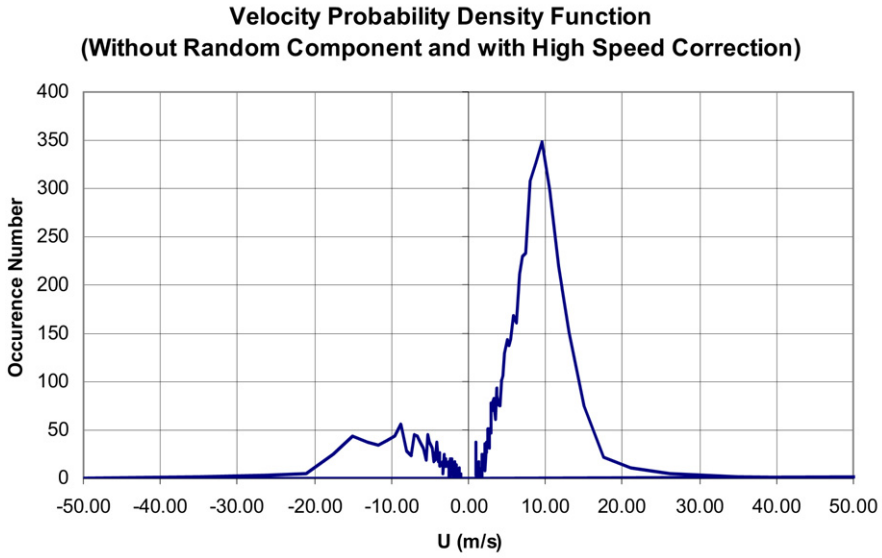

Fig. 14. Final velocity PDF (station 2, $Y = 1$ mm); local velocity evaluated Vmp = 9.54 m/s; local mean velocity evaluated Vmean = 5 m/s.

- From $|U| \geqslant 17$ m/s a speed grid having a 1 m/s step is made, which corresponds roughly to the obtained accuracy approaching 10 m/s.
- Between two successive points, it is assumed that the PDF velocity evolves linearly.

By considering these assumptions, another correction algorithm to the PDF velocity is applied. It consists in generating, between two existing points, fictitious velocity values by respecting a 1 m/s step. Subsequently, all the events corresponding to these two basic points are distributed in a linear way between all the fictitious points. For this, the same population ratio between the two basic points before and after correction was kept. Thus, thanks to this correction, a new oversampled PDF was obtained. It should be noted that the form of this new function depends on the selected accuracy (here, 1 m/s).

After these corrections, we obtain typical PDF velocity such as one presented in Fig. 14.

By applying this treatment to measurements corresponding to the five stations of the experiment, the PDF velocity for all the probed points was evaluated. From these data, we are able to describe the velocity field inside the cavity. For each point, the most probable value of the PDF to define the local velocity was kept.

Experimental results obtained for flow velocity and void ratio fields have been confronted with ones evaluated by numerical simulation. Main results and analyzes are presented here above.

3. Experimental results

The new data processing methods described in Section 2 has been used to process the obtained experimental data set in order to evaluate the void ratio and longitudinal mean velocity fields.

3.1. Void ratio distribution

Figs. 15(a)–(e) show the void ratio evolution against the wall distance Y for the five probed stations. From these results, it is possible to estimate δ the local sheet thickness which corresponds to the zone where the void ratio is greater than 1%. Table 1 shows the measured values of δ for the five probed stations. It is clear

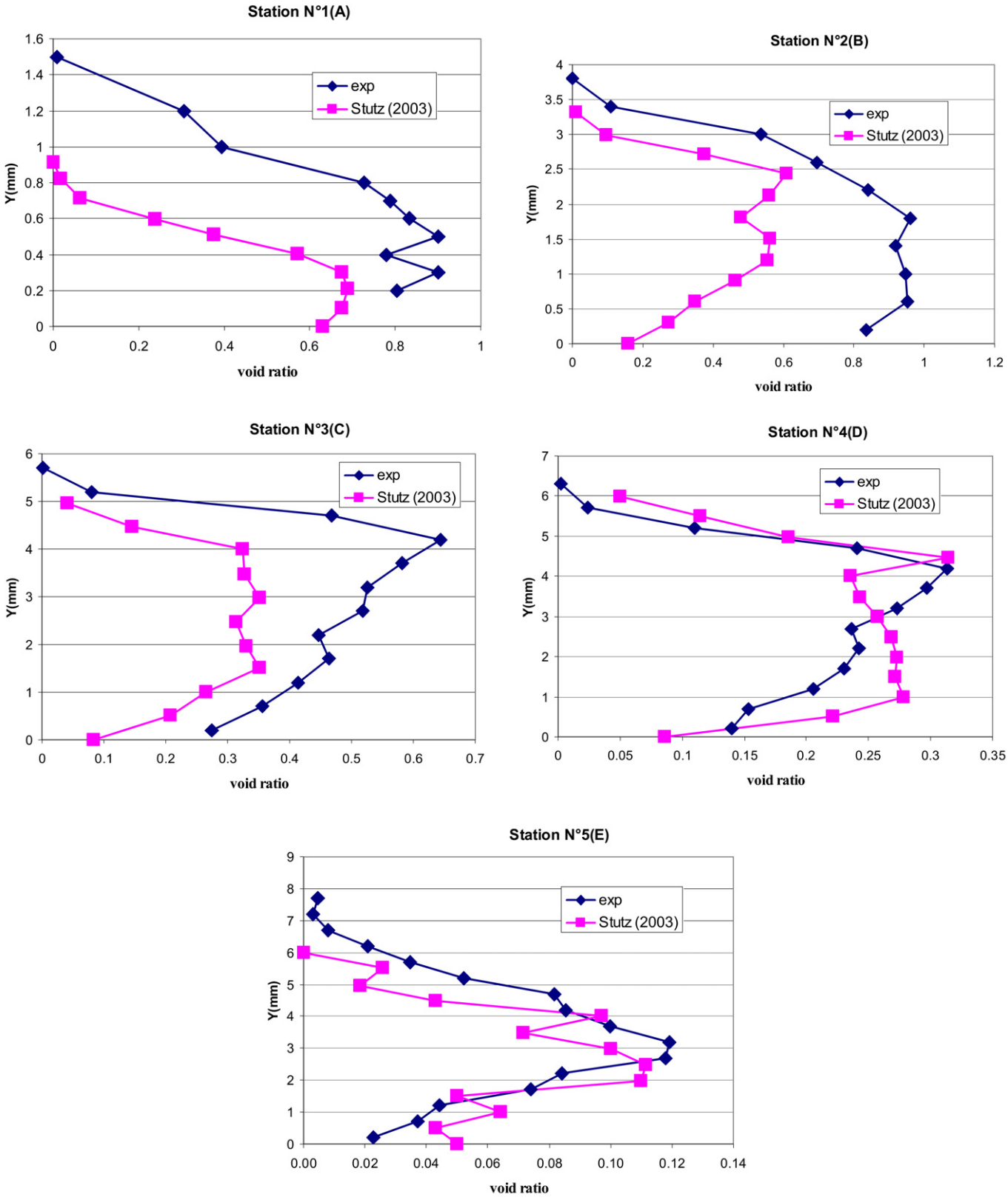

Fig. 15. Experimental void ratio profiles. Station N° 1 (A); Station N° 2 (B); Station N° 3 (C); Station N° 4 (D); Station N° 5 (E).

Table 1
Cavitation sheet thickness for the five probed stations

Station number	1	2	3	4	5
δ (mm)	1.5	3.75	5.65	6	6.6

that for stations N° 2 to 5 the overall agreement with Stutz's results is quite acceptable in terms of cavitation sheet thickness (δ). At the opposite for station N° 1 we found a 50% difference between the two sheet thicknesses. The present experiment was then cross checked and the same results were obtained. At the present time no satisfactory explanation can be given for this discrepancy.

Present results are confronted with Stutz's [4] ones. For stations N° 1–3, the evolutions are qualitatively equivalent. It appears that Stutz's results tend to underestimate the void ratio. On the opposite, for the last two stations (N° 4 and 5), the two sets of results seem to be closer.

The present study indicates very large α values, in the range of 0.9 to 0.95 for stations N° 1 and 2. Concerning the rear part of the cavitation sheet (stations N° 3–5), the maximum void ratio value seems to be shifted roughly to the middle part of the sheet, while in the wall region the void ratio falls drastically. This configuration may be explained by the influence of the re-entrant jet which will be described hereafter in this paper.

3.2. Velocity fields

Figs. 16(a)–(e) show the spatial evolution of the longitudinal velocity for the five probed stations. Three kinds of data are displayed: the results obtained by Stutz [4] concerning most probable velocities, and ones issued from the present experiments presented in terms of mean velocity (Vmean) and most probable velocity (Vmp).

At **station N° 1** (Fig. 16(a)), considering recent data, a velocity profile close to a turbulent boundary layer type is obtained near the wall. For the intermediate region ($0.2 < Y < 0.8$ mm), the velocity is quasi constant. It can be shown that, excepted in the external part of the sheet (for high values of Y), the mean velocities (Vmean) are close to the most probable ones (Vmp). This means that the turbulent field is Gaussian or near-Gaussian at this place which is close to what can be found in the core of a shear layer (a boundary layer in the present case). Obviously, the external boundary corresponds to a highly intermittent zone where mean and most probable velocity diverge.

Stutz's [4] results are in disagreement with the present study. Firstly, in a region close to the wall ($0 < Y < 0.4$ mm) he observed a velocity in the range of 1 to 2 m/s quite close to a re-entrant jet signature. Secondly, in the upper part of the sheet, he observed a quasi boundary layer type profile.

At **station N° 2** (Fig. 16(b)), a great disagreement between analyzed data can be observed. The Vmp profile reaches the external velocity (~ 12 m/s) at the superior boundary of the sheet. We can also observe a constant Vmp ≈ 10 m/s zone for ($1 < Y < 2.5$ mm) and, for lower values of Y, a boundary layer profile is obtained, which may correspond to the initial boundary layer observed in station N° 1. According to these results, a sheared zone seems to occur in the external part of the sheet in this flow region. This shear does not appear on Vmp profile at station N° 1. The Vmean profile is qualitatively comparable to the Vmp one in the external part of the sheet ($1.5 < Y < 3.5$ mm). On the opposite, in the turbulent zone closer to the wall the difference between Vmean and Vmp increases: the strong structural difference observed between Vmean and Vmp profiles in this region seems to indicate that the turbulent field is far from Gaussian and that the re-entrant jet has an effect on the flow structure even if it is not really visible at station N° 2. From Stutz's [4] results, a re-entrant jet may be observed at station N° 2, expanding until $Y \sim 1.5$ mm.

In the rear part of the sheet (**stations N° 3, 4 and 5** on Figs. 16(c)–(e)) a re-entrant jet is clearly visible from the Vmp profile. At station 3, we can observe a good qualitative agreement between the Vmp profiles and Stutz's [4] ones: for both studies, the re-entrant jet thickness is found equal to about 2.5 mm. As observed before, at station N° 2 (Fig. 16(b)), the core of a free shear layer is located at $Y = 2.5$ mm, near the sheet external boundary. It seems that this layer is the starting point of the detachment process of the internal sheet flow. This free shear layer is observed at station N° 3 in the range of ($2 < Y < 3$ mm) and corresponds to the boundary between the main flow (external) and the re-entrant jet.

The Vmean experimental profile is different both in shape and values from the Vmp one. Indeed, in the re-entrant jet zone the flow is strongly turbulent with a lot of large scale fluctuations (unsteadiness). The turbulent field is very complex with reversed flow, intermittent boundaries and is remote from a Gaussian one. In fact, the re-entrant jet is not well described by the Vmean profile because, in the free shear layer zone ($Y \approx 2.5$ mm), the flow is greatly intermittent and the PDF velocity in this zone showed a kind of two-state systems oscillating between a positive and a negative value of the velocity (typically Vmp switches between $\mathrm{Vmp}^- = -2$ m/s and $\mathrm{Vmp}^+ = 8$ m/s). Due to this situation, in this region Vmean only represents the mean of these two values with a variable "weighting" depending on the respective probability of occurrence of Vmp^- and Vmp^+ at each Y positions. The boundary of the re-entrant jet may then be defined by the place where the occurrences of these two values on the PDF velocity are equal. In this case Vmean can be simply computed as the mean of Vmp^- and Vmp^+, that is Vmean $= 3$ m/s which corresponds roughly to $Y = 2.5$ mm (see Fig. 16(c)).

When comparing the present Vmp profiles with Stutz's one at stations N° 4 and 5, we observe that both re-entrant jet thickness and velocity are found very different. These high discrepancies may be attributed to the huge difference on the observation time between the present work and Stutz's one, mainly in the re-entrant jet zone where the intermittency of the flow makes the convergence of statistics difficult. Moreover, it is also possible to explain these differences by the quite drastic changes on the velocity computation algorithm performed in the present study. It is worth noting that the new velocity field structure obtained from the present experiments leads to a new flow rate repartition in the cavitation sheet as compared to the one obtained by Stutz [4].

4. Numerical code

4.1. Multiphase equation system

In collaboration with Numeca International, the LEGI laboratory has implemented cavitation models in the Fine/Turbo™ code. The numerical tool is a three-dimensional structured mesh code that solves Reynolds-averaged Navier–Stokes equations. A detailed description of the initial code is given in Hakimi [29].

The governing equations are written for a homogeneous fluid. This fluid is characterized by a density that varies in the two-phase mixture zone according to a barotropic state law and that is related to the void ratio "α" by the equation:

$$\rho_m = \alpha\rho_v + (1-\alpha)\rho_L$$

where ρ_m is the mixture specific mass, ρ_v is the vapor specific mass and ρ_L is the liquid one. Each pure phase is considered incompressible.

The void ratio characterizes the volume of vapor in each cell: $\alpha = 1$ means that the cell is completely occupied by vapor

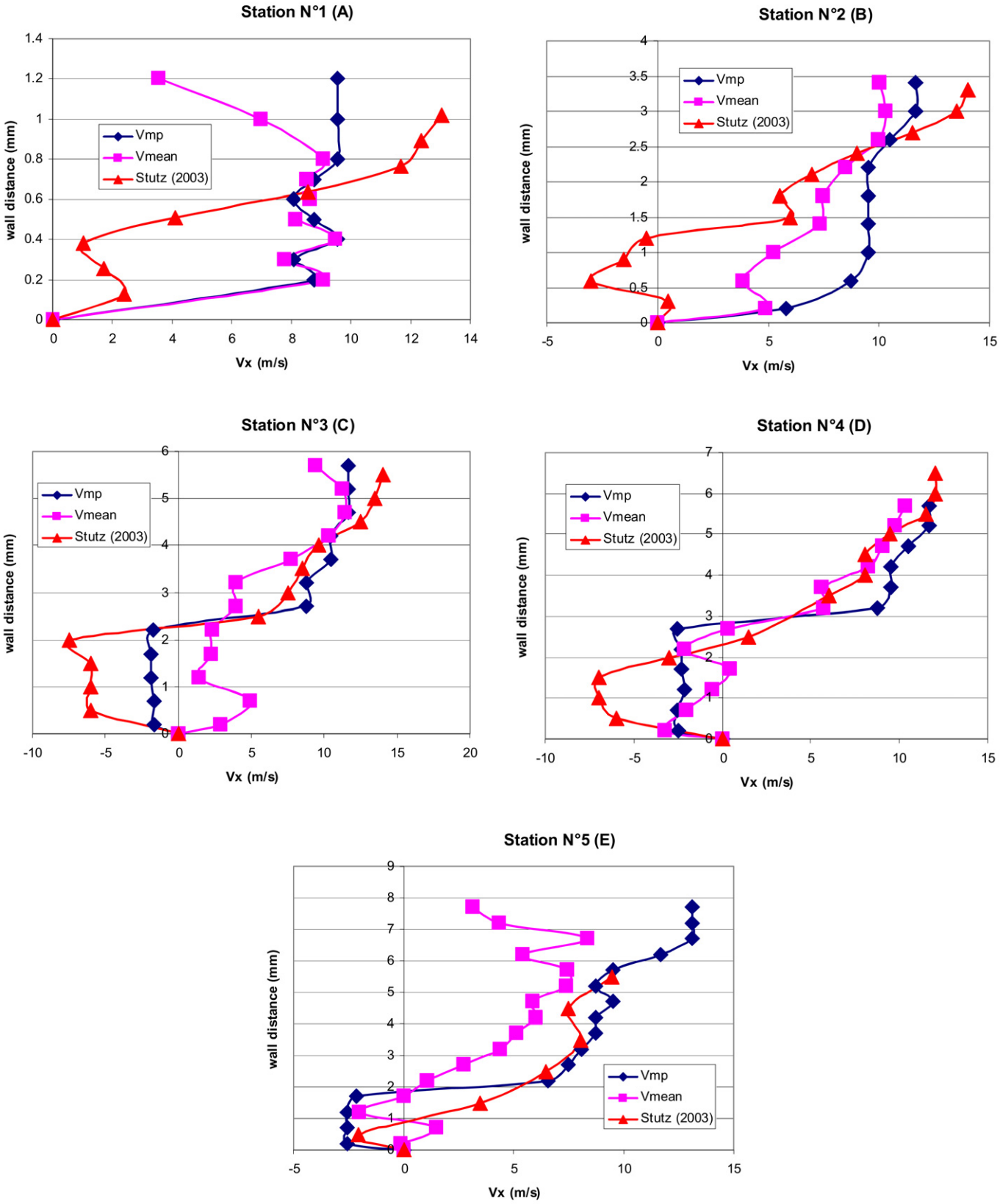

Fig. 16. Experimental velocity profiles. Station Nº 1 (A); Station Nº 2 (B); Station Nº 3 (C); Station Nº 4 (D); Station Nº 5 (E).

($\rho_m = \rho_v$); inversely, a complete liquid cell is represented by $\alpha = 0$ ($\rho_m = \rho_L$). Liquid and vapor phases are characterized by their thermodynamic properties. On each cell, the unknowns are calculated by averaging them by the volume occupied.

In this homogeneous model, the transfers between the two phases are implicitly treated. The two phases are considered to be locally (in each cell) in a dynamic equilibrium (no drift velocity).

The steady compressible Reynolds-averaged Navier–Stokes equations are expressed as:

$$\nabla \cdot (\rho_m \mathbf{u}_m) = 0,$$

$$\nabla \cdot (\rho_m \mathbf{u}_m \otimes \mathbf{u}_m) = -\nabla(p_m) + \nabla \cdot (\bar{\bar{\tau}}_m) + \rho_m \mathbf{F}_m$$

where $\bar{\bar{\tau}}_m$ is the shear stress tensor and $\mathbf{F}_m$ is the body forces (equal to zero in the present application).

The space discretization is based on a cell-centered finite-volume approach. The numerical convective fluxes are computed with a second-order central scheme stabilized by the Jameson dissipation (Jameson et al. [30]).

Pseudo-time derivative terms are added to the equations. They enable equation convergence to steady state. The explicit four stage Runge–Kutta time stepping procedure is used to advance the solution to steady state.

A complete description of the numerical scheme is presented by Coutier-Delgosha et al. [7].

4.2. Preconditioned Navier–Stokes equations

In the case of low-compressible or incompressible flows, the time-marching algorithm converges very slowly and the use of a low Mach number preconditioner in the Navier–Stokes equations is required (Turkel [31], Hakimi [29]). It is based on the modification of the pseudo-time derivative terms in the governing equations. Such modifications have no influence on the converged results, since these terms are of no physical meaning, and converge to zero. The resulting preconditioned system is controlled by pseudo-acoustic eigenvalues much closer to the advective speed, reducing the eigenvalue stiffness and enhancing the convergence.

Using this preconditioner in the case of steady calculations, the set of equations becomes:

$$\iiint_V \bar{\bar{\Gamma}}^{-1} \frac{\partial \mathbf{P}}{\partial \tau} dV + \iint_\Sigma \mathbf{F} \cdot \mathbf{n} \, d\Sigma = \iiint_V \mathbf{S} dV.$$

Flux vector $\mathbf{F}$ can be decomposed in an inviscid and a viscous part,

$$\mathbf{F} = \mathbf{F}_I - \mathbf{F}_V$$

with

$$\mathbf{F}_I = \begin{pmatrix} \rho \mathbf{u} \\ \rho(\mathbf{u} \otimes \mathbf{u}) + p\bar{\bar{I}} \end{pmatrix} \quad \text{and} \quad \mathbf{F}_V = \begin{pmatrix} 0 \\ \bar{\bar{\tau}} \end{pmatrix}.$$

Vector $\mathbf{S}$ represents the source term (equal to zero in the present study).

The preconditioning matrix $\bar{\bar{\Gamma}}^{-1}$ and associated variable vector $\mathbf{P}$ are given by:

$$\mathbf{P} = \begin{pmatrix} p_g \\ \mathbf{u} \end{pmatrix} \quad \text{and} \quad \bar{\bar{\Gamma}}^{-1} = \begin{pmatrix} 1/\beta^2 & 0 \\ (1+\alpha)\mathbf{u}/\beta^2 & \rho \end{pmatrix}$$

where p_g is the gauge (relative) pressure, $\mathbf{u}$ is the velocity vector, α and β are the preconditioning parameters. In the present applications, $\alpha = -1$ and β depends on the reference velocity, and is defined by: $\beta^2 = \beta_0 \cdot U_{ref}^2$ with $\beta_0 = 3$ in our case.

The eigenvalues of the preconditioned system become:

Table 2
Physical parameters and tested Amin values

	T (K)	ρ_v kg/m^3	ρ_l kg/m^3	Amin m/s(kg/m^3)$^{0.5}$	c_{min} m/s
Water	293	0.0173	998	70	3.13
				50	2.24
				20	0.89

$$\lambda_1 = \mathbf{u} \cdot \mathbf{n} \quad \text{and}$$

$$\lambda_{2,3} = \frac{1}{2}\left[\mathbf{u} \cdot \mathbf{n}(1-\alpha) \pm \sqrt{(\mathbf{u} \cdot \mathbf{n}(1-\alpha))^2 + 4\mathbf{n}^2\beta^2}\right]$$

where $\mathbf{n}$ is the normal vector to the elementary surface dS.

For more details concerning the used preconditioner, see Coutier-Delgosha et al. [25].

4.3. Turbulence models

In the present work, the Yang–Shih k–ε model (Yang and Shih [32]) with extended wall functions (Hakimi et al. [33]) has been applied.

4.4. Barotropic model

To model cavitation phenomenon and to close the governing equations system, a barotropic state law introduced by Delannoy and Kueny [19] has been implemented in Fine/Turbo^{TM} code (Pouffary [5,6,18], Coutier-Delgosha et al. [7,25]). The fluid density (and thus the void fraction) is controlled by a law $\rho(p)$ that links explicitly the mixture fluid density to the local static pressure as represented in Fig. 17.

This law is mainly controlled by its maximum slope, which is related to the minimum speed of sound c_{min} in the mixture. Parameter Amin controls this slope:

$$AMIN^2 = \frac{\rho_L - \rho_V}{2} c_{min}^2.$$

Table 2 presents Amin values used for cold water calculations presented in this paper. Thermodynamic effects have been neglected and the energy equation was not taken into account. Works are in progress in order to implement new cavitation models including thermal effects (Rolland et al. [34,35]).

In relation to the study presented in [7] concerning the same geometry and the same numerical tool, meaningful numerical work has been performed by Pouffary [36], Numeca International and Rolland [35] to improve the preconditioner and the stability of the numerical code for calculations of cavitating flows. It is worth noting that these numerical modifications led to major improvements in accuracy and numerical stability in comparison with our previous computations of cavitating flows [7]. We underline also that, thanks to recent numerical modifications, calculations considering stiffer slopes of barotropic law (corresponding to $c_{min} < 1$ m/s) can now be performed.

Moreover, in complement to previous works, the present study focuses on local analyzes of flow parameters (pressure, velocity and void ratio fields) and on a quantitative evaluation of the influence of barotropic model characteristic parameter Amin on the local steady results obtained.

5. Experiments-simulation confrontation in cold water

5.1. Calculation conditions

The studied case, presented in Section 1, is a quasi-stable sheet with a length of about 80 mm, at $U_{inlet} = 10.8$ m/s. The reference

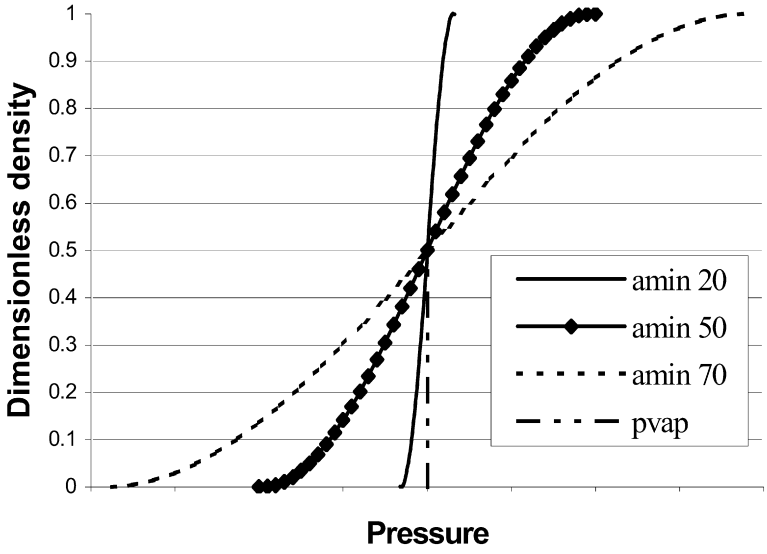

Fig. 17. Influence of Amin parameter on barotropic law.

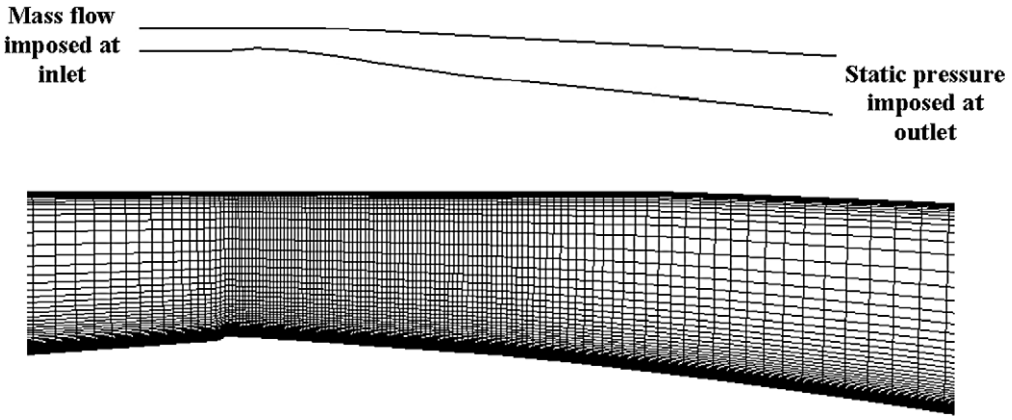

Fig. 18. Views of mesh for k–ε computational: (a) total domain and imposed boundary conditions; (b) zoom near the Venturi throat.

Table 3
Comparison of experimental and simulation values of the sheet length (L) versus the cavitation parameter σ

Amin	70	50	20	*exp*
Sigma (inlet)	0.683	0.642	0.600	0.547
L_{sheet} (mm)	79.8	80.2	81.5	80
Vapor volume ($\times 10^{-4}$ m^3)	4.005	3.741	3.699	

density is the liquid density equal to 998 kg/m^3. Steady calculations are led with the k–ε turbulence model, with extended wall functions.

For the Venturi geometry studied and numerical tool applied in this paper, mesh tests were presented in reference [7]. The 2D mesh used in the present work, illustrated in Fig. 18, contains 9861 nodes, 173 in the flow direction and 57 in the normal direction. As reported in [7], such grid size is adequate to simulate the steady sheet cavitation in this Venturi type section.

The $y+$ values vary from 18 to 50. The boundary conditions are mass flow for inlet condition and static pressure imposed at outlet.

5.2. Global analyzes

Initially, we have analyzed the cavity global behavior, mainly the sheet length as a function of the cavitation number. In order to carry out comparisons with experimental data, three calculations with different Amin values are considered in this paper. They have been conducted by trial and error to obtain almost the same sheet length. A smooth variation of the inlet cavitation number is observed (see Table 3).

The influence of Amin on the sheet vapor volume seems weak. Nevertheless, according to Fig. 19, for a same cavity length, an increase of Amin leads to an augmentation of the cavity thickness. Indeed, this parameter controls the maximum slope of the barotropic law: for high values of Amin, the maximum slope decreases, resulting in a smoothing of the density gradients and in an augmentation of diffusive effects. As shown in Fig. 19, the upper part of the sheet interface is more diffuse for the higher Amin values. Local analysis, presented in the next section, has confirmed these tendencies.

The defined sheet length used for representing the computational results has been determined by the length of the isoline corresponding to a void ratio $\alpha = 0.3$. This criterion is argued by the fact that it corresponds to the area of maximal value of the density gradient (see Fig. 20). As a matter of fact, because of the strong density gradient at the enclosure of the sheet, the sheet length varies weakly as a function of the interface criterion. A test showed that, for a void ratio between 10% and 30%, the sheet length variation was about 2%.

From the analyzes of streamlines plotted in Fig. 19, we observe for Amin = 20 a re-circulation zone in the sheet wake, which is almost inexistent for higher values of Amin. As it will be illus-

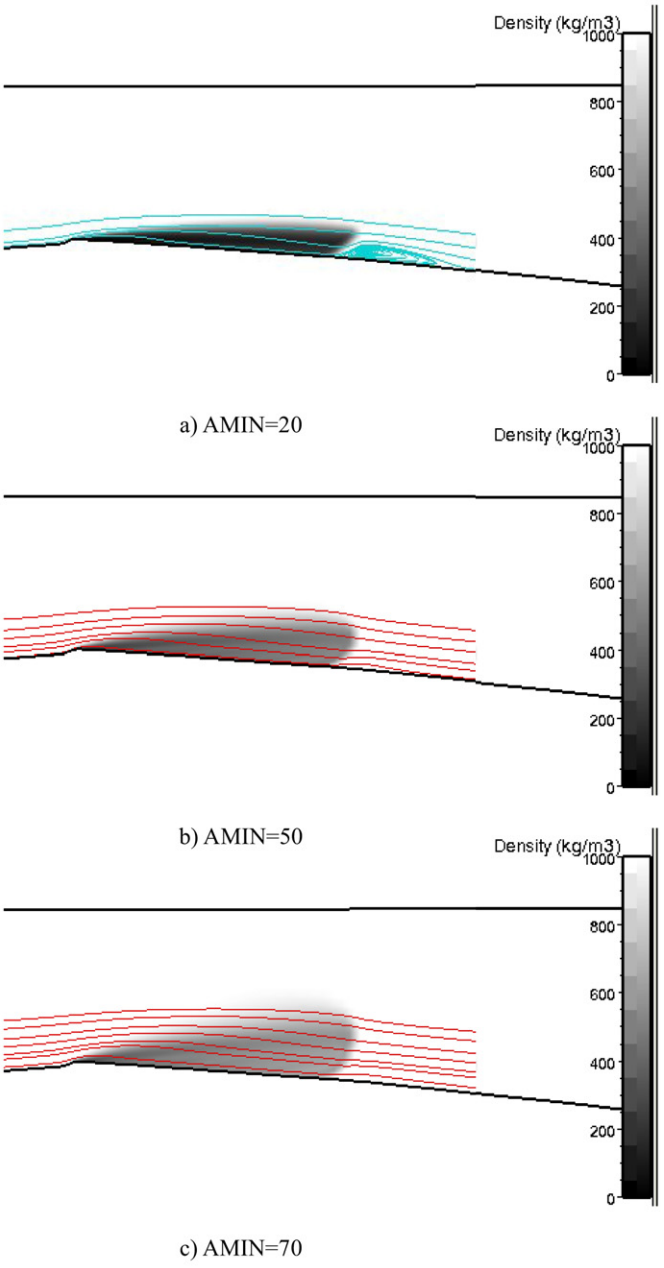

Fig. 19. Calculated density field inside the cavity and streamlines.

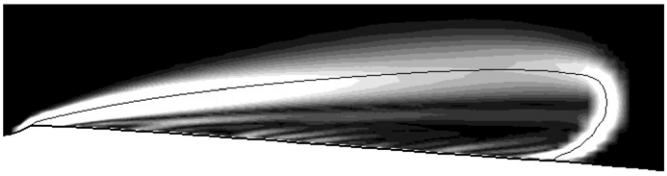

Fig. 20. Magnitude of density gradient (0 to 10^6 kg/m^4) and iso-line $\alpha = 0.3$ $L_{\text{sheet}} \sim 80$ mm, Amin = 50.

trated in the next sections, this re-circulation phenomenon affects the pressure distribution at the Venturi lower wall.

5.3. Local analyzes

This part focuses on the analyzes of local void ratios and velocity profiles inside the cavity, as well as of the wall pressure distribution. The void ratio and velocity profiles are obtained for the five stations defined in Section 1 of the paper. New experimental results will be confronted to the numerical simulation data obtained in the present work as described in part 2 and 3 hereafter.

Original analyzes of the flow structure and the pressure distribution at the Venturi wall obtained from this combined experimental and numerical work are also presented in the following sections.

5.3.1. Void ratio distribution

Figs. 21(a)–(e) show the void ratio evolution for the five probed stations. Present experimental results are compared to computation data obtained with three different values of the Amin (Amin = 20, 50 and 70) parameter in the barotropic law used to model the phase change during vaporization and condensation process.

At stations N^o 1 and 2 (Fig. 21 (a) and (b)) a satisfactory agreement is obtained between experimental void ratio values and those issued from computations with Amin = 20. It can be also shown that an increase on the Amin value leads to an underestimation of the void ratio near the wall and also predicts an overestimation of the sheet thickness as compared to the experimental observations. For example at station N^o 1, we measured a sheet thickness $\delta = 1.5$ mm, while computations using Amin = 50 and 70 respectively give value of 3 to 4 mm for δ. It seems that almost in the initial part of the sheet (stations N^o 1 and 2) the barotropic law with Amin = 20 (leading to a minimum sound velocity Cmin = 0.89 m/s) is able to model quite accurately the flow behavior in the leading part of the sheet where the flow is stable, with no counter-current component and with a relatively high void ratio due to the strong vaporization process occurring here. On the opposite, from stations N^o 3 to 5 the situation is different. While going downstream, the disagreement between experiments and computation increases culminating at station N^o 5 where the discrepancies on the maximum value of the void ratio may reach 800% in the worse case (here, Amin = 20). Computations both overestimate void ratio and sheet thickness in this flow zone. We note that, during experiments, the cavity length fluctuates: 70 mm $< L <$ 85 mm. Station N^o 5 is placed at $\sim$74 mm and quantitative comparisons in this zone are very tricky.

5.3.2. Flow velocity fields

We can explain the precedent discrepancies also by analyzing Figs. 22(a)–(e), where velocity profiles are presented for the five probed stations. On these figures, the velocities issued from the present experiment (Vmean and Vmp) are compared to those obtained by computations with Amin = 20, 50 and 70. The analysis is split in two parts. The first one concerns stations N^o 1 and 2 and the second one, stations N^o 3–5.

Simulation results exhibit a strong sensibility on the value of the Amin parameter. However, the velocity profiles are qualitatively comparable and are close to a turbulent boundary layer type profile. It is found that the Amin = 20 profile seems to best fit the experimental data at station N^o 1.

At station N^o 2, the comparison between experimental and numerical velocity profiles leads us to the conclusion that the simulation performed with Amin = 20 is the one that fits the experimental results better (at least concerning the Vmp profile). However, the computed profiles are of the turbulent boundary layer type. They differ from the experimental ones, both on the velocity values obtained and on the shape of the profiles. It can also be noticed that in station N^o 2, the maximum values for void ratio are attained, showing that the vaporization phase ends near station N^o 2 and that the Vmp profile seems to be a precursor of the ones which will be obtained downstream due to the effect of the adverse pressure gradient imposed by the flow geometry. (This fact is firstly illustrated in Fig. 22(c) where the experimental and com-

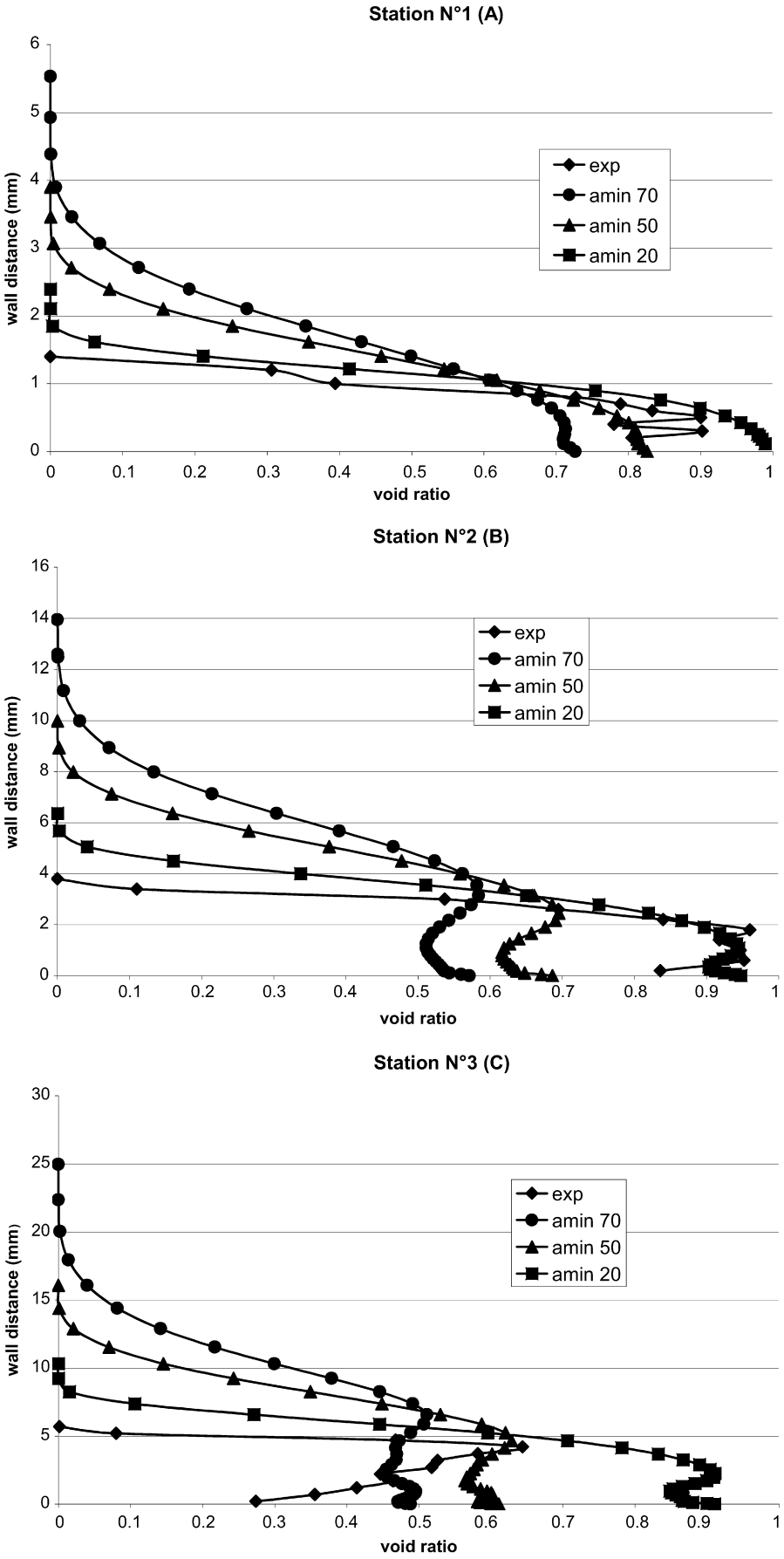

Fig. 21. Void ratio profiles: comparison between present experiments and simulation results.

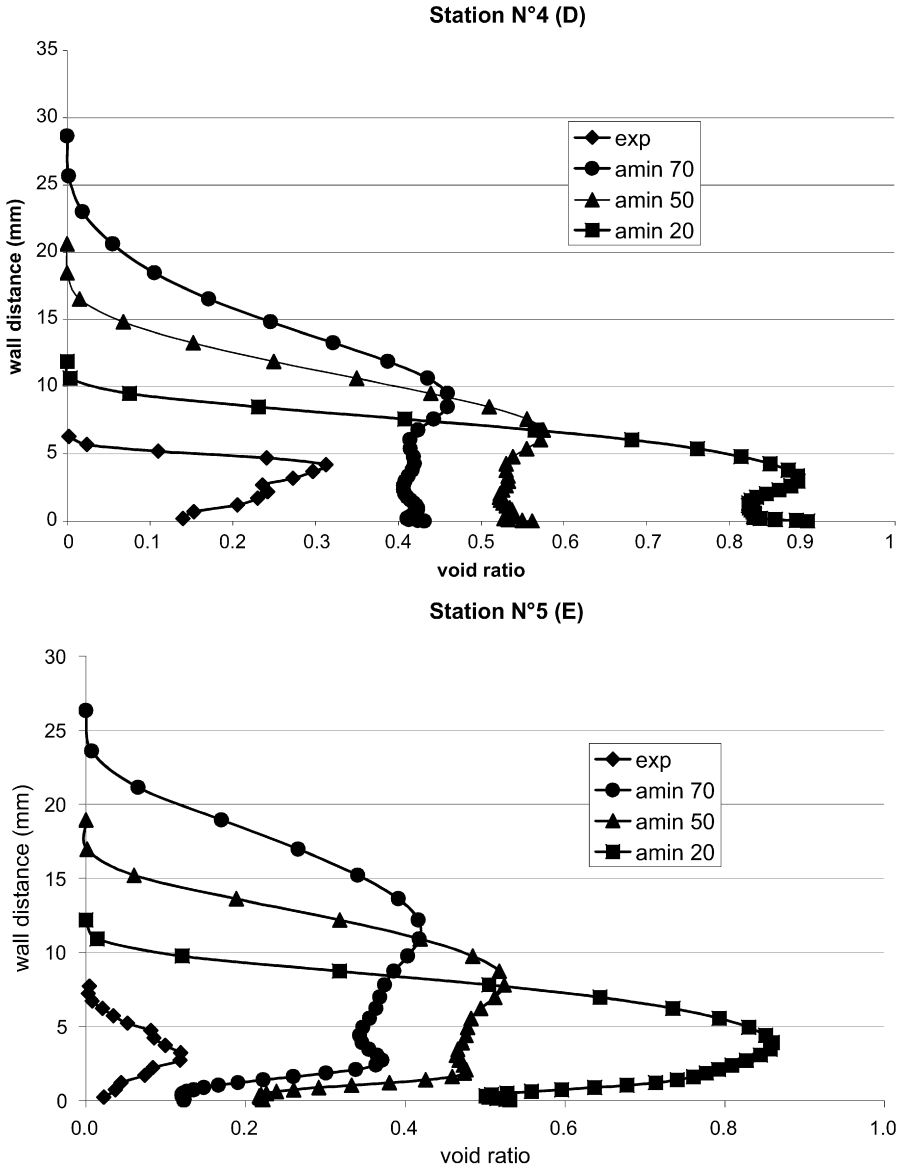

Fig. 21. (*Continued.*)

putational velocity profiles are represented.) It is important to note that numerical results obtained in stations N° 1 and N° 2 with a steady approach are similar (even better) to the ones achieved by Reboud et al. [20] from unsteady computations by using code "IZ" and $c_{\min} \sim 1$ m/s.

Numerical simulation at station N° 3 (Fig. 22(c)) always shows boundary layer type profiles. The Amin = 20 case is the less remote from the experimental results, but, in any case, stable simulation is not able to predict the re-entrant jet structure. Concerning stations N° 4 and 5 (Fig. 22 (d) and (e)) the situation is similar to the one described for station N° 3. The purely stationary aspect of the simulation used here is not able to describe the rear part of the cavitation sheet accurately because it does not take into account the strong unsteady aspects of this flow, mainly due to the re-entrant jet phenomenon. Nevertheless, it is worth underlining that, for Amin = 20, quantitative predictions of sheet thickness, velocity and void ratio local fields in the upstream zone corresponding to a stable behavior of the cavity are in very good agreement with experimental results.

5.3.3. Analyzes of flow structure

Simultaneous analyzes of void ratio and velocity fields enable the improvement of study of the considered cavitating flow.

Based on numerical results illustrated in Fig. 19, we will consider that iso Y lines represent streamlines inside the cavity. Fig. 23(a) represents the void ratio longitudinal evolution measured for five values of distance Y from the wall ($Y = 1.2$ mm, 2.2 mm, 3.2 mm, 4.2 mm and 5.2 mm) at the five stations considered. The values X (horizontal axis) shown in Fig. 23(a) express the downstream distance from the Venturi throat which is located at $X = 0$. The position of the five probed stations is represented by the dots on the figure. The three isolines $Y = 3.2$ mm, 4.2 mm and 5.2 mm correspond to the upper part of the sheet, where the flow is running in the main flow direction everywhere in the cavitation sheet. For the other values of distance Y, the flow runs in the main direction for stations N° 1 and 2, and in the opposite way (reversed flow corresponding to re-entrant jet) for stations N° 3–5.

For $Y = 4.2$ mm, it can be noted that a strong vaporization occurs between stations N° 2 and 3, followed by a less violent condensation process when entering in the recompression zone of the flow (stations 3–5).

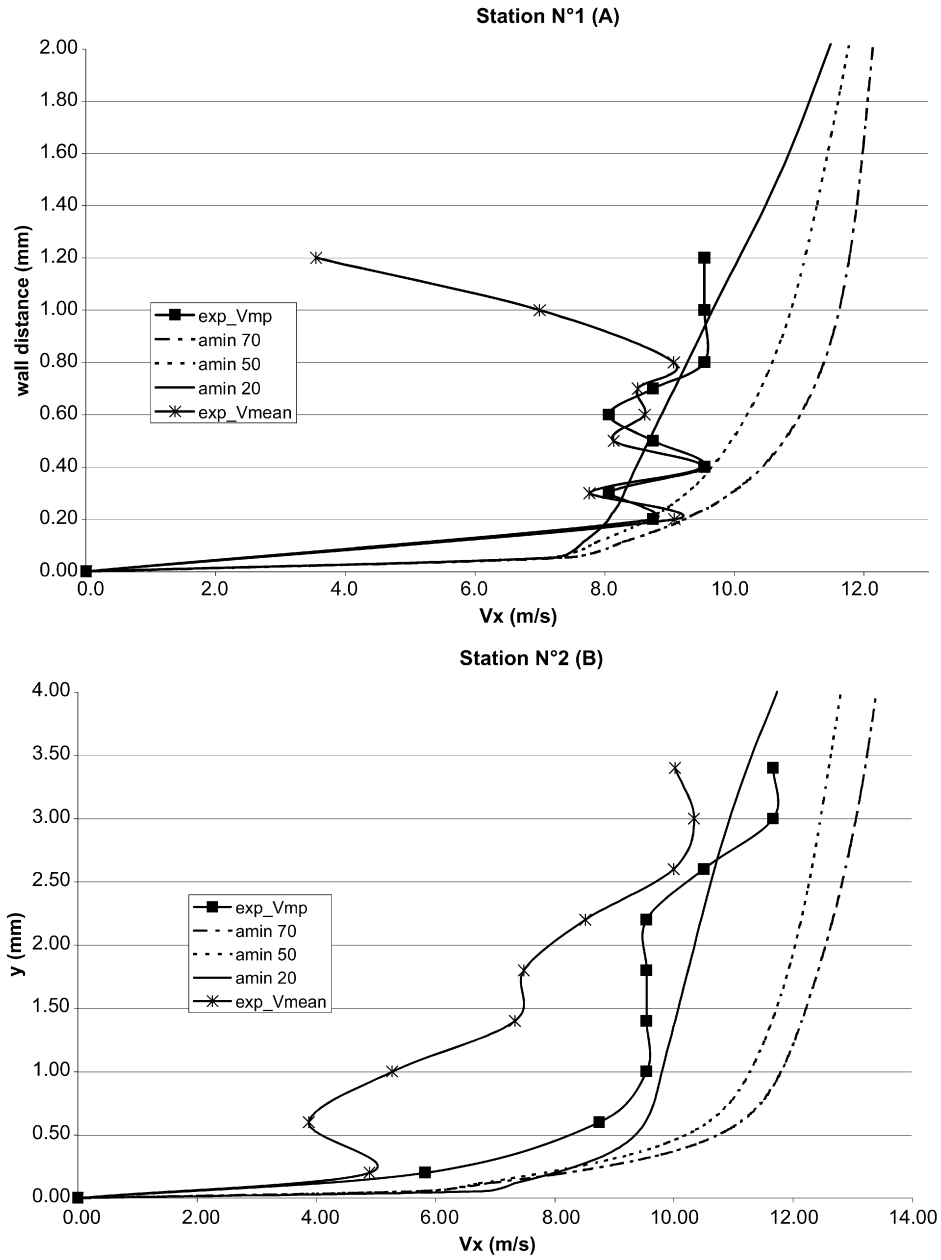

Fig. 22. Velocity profiles: comparison between experimental and simulation results. Station N° 1 (A); Station N° 2 (B); Station N° 3 (C); Station N° 4 (D); Station N° 5 (E).

For the streamlines corresponding to $Y = 1.2$ mm and 2.2 mm (which are related to the re-entrant jet at stations N° 3–5), the upstream zone ($0 < x < 20$ mm) exhibits also a strong and fast vaporization process, mainly between stations N° 1 and N° 2. The downstream zone ($38 < x < 74$ mm) corresponds to the re-entrant jet vaporization zone (the flow is running in the rear direction here), which seems to be quite slower than the initial process occurring at the leading edge of the sheet. It can be noticed that for all the studied isolines the void ratio seems to converge to values in the range of 5 to 12% at station N° 5, which determines the initial condition of the re-entrant jet.

Results obtained from numerical calculations with Amin = 20 are plotted in Fig. 23(b) in the stable upstream zone of the cavity ($0 < x < 40$ mm). It is interesting to note that the strong vaporization phenomenon observed in this zone from experimental measurements recalled in Fig. 23(b) is very well predicted by simulations, mainly for $Y = 1.2$ mm, 2.2 mm and 4.2 mm isolines.

5.3.4. Wall pressures

Because 3D unsteady calculations of cavitating flows are very time-consuming, a steady approach to simulate the global performances of pumps under cavitating conditions is applied. As a first step to evaluate the prediction capability of the calculation methodology applied, experimental and simulated pressure distribution at the Venturi wall have been analyzed and compared.

Fig. 24 represents the mean wall pressure longitudinal evolution. The ratio $(p - p_v)/p_v$, where p is the local wall pressure and p_v is the vapor pressure, is plotted versus $x - x_i$, where $x - x_i$ is the distance between the measuring station and entry section (S_i). This experimental result is confronted on Fig. 24 with the simulation result obtained with different Amin values. A most important difference between simulation results is observed in the sheet wake. As illustrated in Fig. 19, for Amin = 20, calculations indicate a re circulation zone that is almost inexistent for higher values of Amin. By comparison with experimental results, the existence of this re-circulation zone leads to a better prediction of

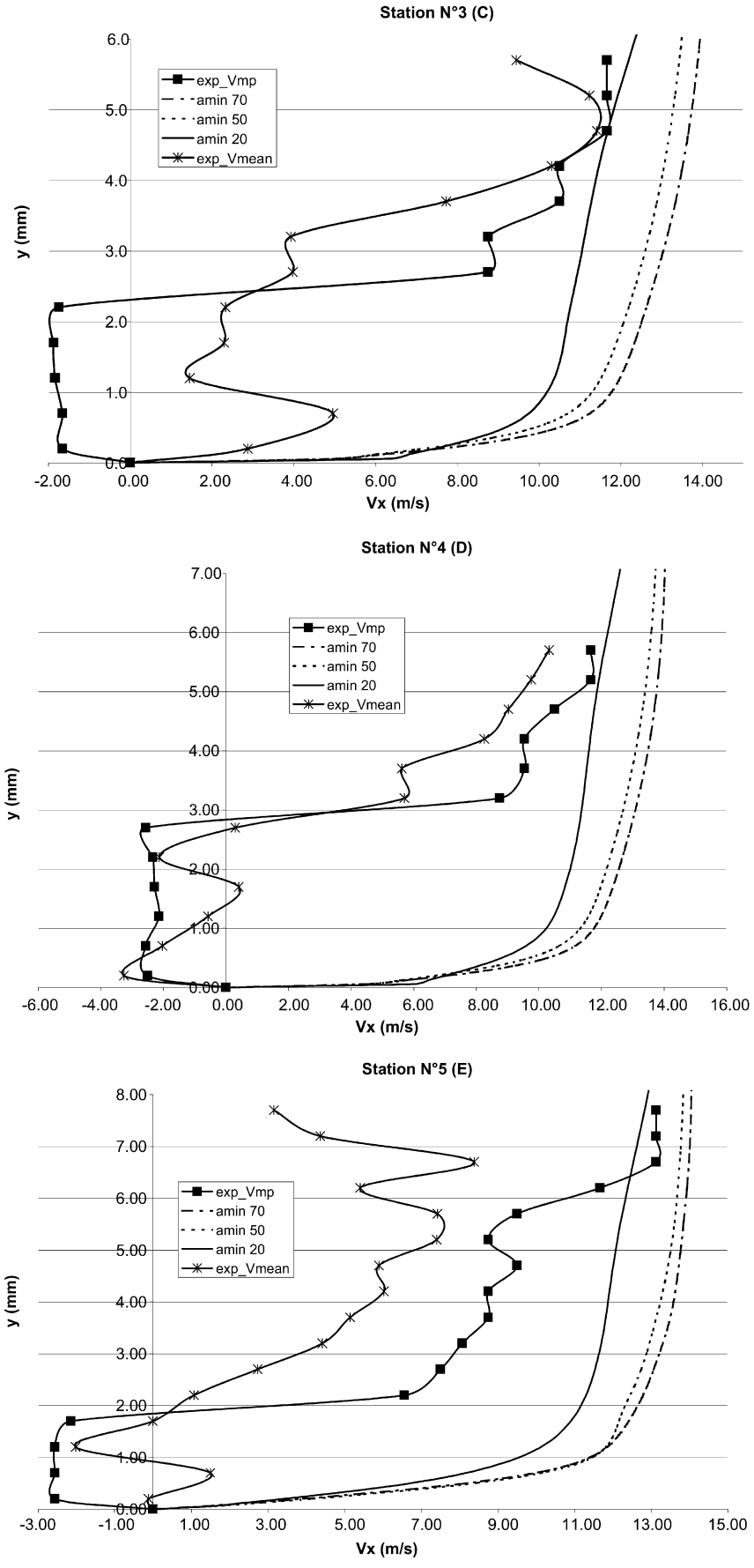

Fig. 22. (*Continued.*)

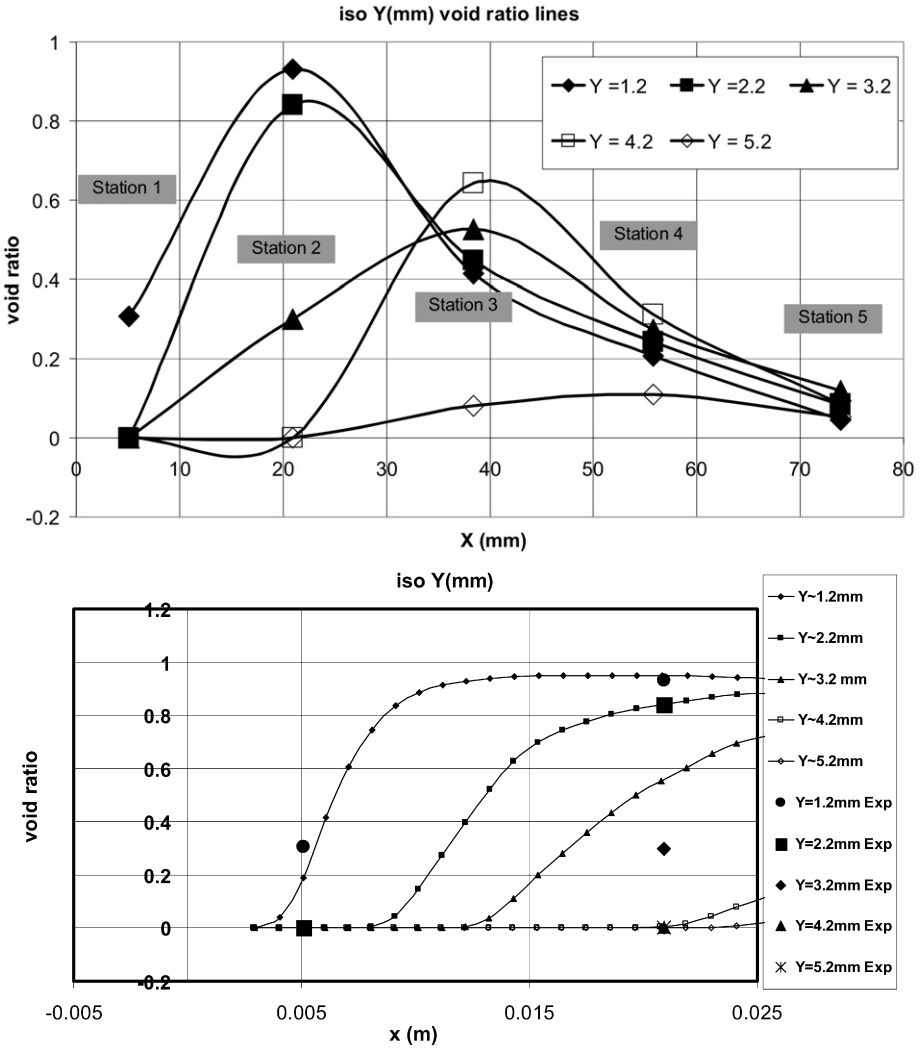

Fig. 23. (a) Iso *Y* void ratio lines from present experimental data. (b): Iso *Y* void ratio lines both from experimental data and numerical simulation (Amin = 20).

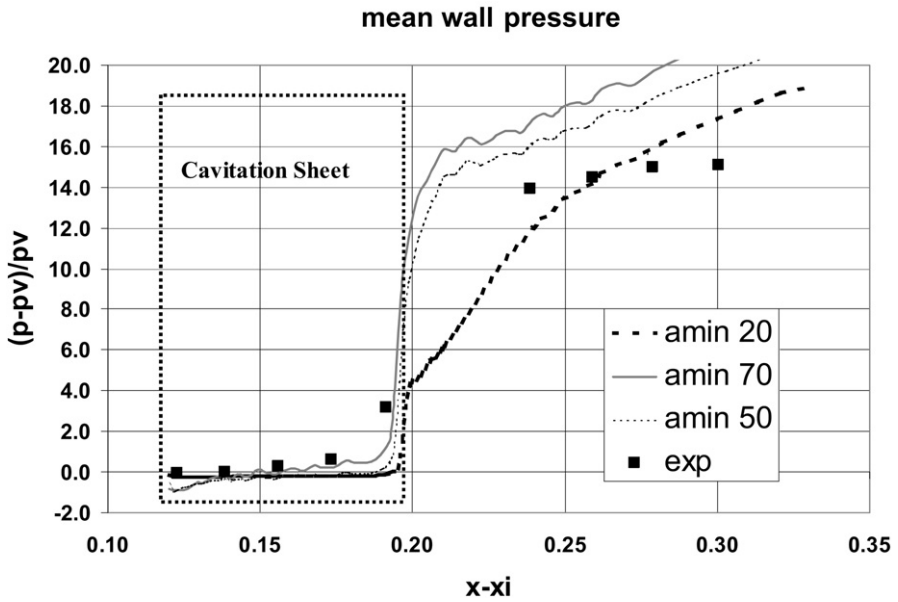

Fig. 24. Longitudinal mean wall pressure evolution: comparison between experimental and simulation results (each square point on experimental curve represents results from station N° 1 [at left] to station N° 9 [at right]).

pressure distribution at the Venturi lower wall in the zone of sheet wake.

Moreover, in the initial part of the sheet (up to station N° 2) the numerical prediction with Amin = 20 fits with measurements quite well giving a wall pressure very close to the vapor pressure. This is not surprising because in all the present paper it has been observed that this zone is well described by the present simulation in terms of void ratio and velocity profiles. On the opposite, in the rear part of the sheet (stations N° 3–9) results are diverging: experimental results indicate a more rapid recompression process than the one predicted by numerical simulation with Amin = 20. Nevertheless, simulations done with Amin = 70 provide better results in the sheet closure region. As a matter of fact, for higher Amin values, the barotropic law is wider and it leads to a condensation delay, which is very small for Amin = 20.

The pressure gradient in the recompression zone between stations N° 5 and 7 is quite well predicted by simulations with Amin = 20. Further downstream, for stations N° 7–9, in the wake area, experimental data exhibits a constant pressure zone linked to the convective wake of rotational structures ejected at the trailing edge of the cavitation sheet due to the re-entrant jet dynamics. In this region, numerical simulations indicate a turbulent boundary layer velocity profile related to the adverse pressure gradient. As a matter of fact, the calculated wall pressure illustrates the pressure gradient imposed by the Venturi geometry and does not take into account the unsteady aspects of the flow at the trailing edge of the cavitation sheet.

In spite of discrepancies observed in flow velocity and void ratio fields between steady calculations and experimental results in the rear part of the cavitation sheet, numerical results obtained in the stable zone of cavitation are in good agreement with experimental ones. Moreover, pressure longitudinal evolution simulated at the Venturi wall is also in quite good agreement with measured mean pressure values.

Further work is required to study the influence of cavitation unsteady behavior on pressure and viscous forces on the solid walls.

6. Conclusion

From double probe measurements and numerical calculations, we have analyzed the global and the local behavior of a cavitating flow through a Venturi geometry. For a quasi-steady cavitation sheet with a length of about 80 mm, we have evaluated void ratio and velocity fields for cold water cavitation.

Experimental measurements and data treatment have been improved for cold water tests. The new method proposed for data analysis leads to a better evaluation of local behavior of steady and unsteady cavitation.

Discussions and conclusions have been drawn from a combined experimental and numerical work. In relation to previous numerical works, original analyzes based on steady calculation concerned mainly wall pressure evolution and a detailed study of the influence of the Amin parameter on void ratio and velocity profiles.

The applied barotropic model, if associated with a stiff slope (corresponding to $c_{\min} \sim 1$ m/s for cold water), seems to predict local behavior in the steady areas of cavitation well. Although the global behavior of the sheet seems steady, experimental data show a re-entrant jet which creates small cloud shedding. In the zones influenced by the re-entrant jet, in spite of discrepancies observed between numerical and experimental flow velocity and void ratio fields, simulated wall pressure longitudinal distribution appears in rather good agreement with measured values.

Additional works are in progress to analyze the influence of physical models and numerical schemes on the cavitating flow behavior simulated. Moreover, numerical work has been performed in order to implement cavitation models including thermal effects in Fine-Turbo™ code (Rolland et al. [34,35]). The present Venturi geometry has been tested by (Frumann et al. [37], Merle [38]) in R114 refrigerant and will be applied as a test case to validate/calibrate models and study thermal effects on cavitation phenomena.

Acknowledgements

The authors wish to express their gratitude to French space agency CNES and to Snecma's DMS to support this research. The authors wish also to express their gratitude to Numeca International for its cooperation to the development of the numerical code.

References

[1] B. Stutz, J.L. Reboud, Two-phase flow structure of sheet cavitation, Phys. Fluids 9 (12) (1997) 3678–3686.
[2] B. Stutz, J.L. Reboud, Experiments one unsteady cavitation, Exp. Fluids 22 (1997) 191–198.
[3] B. Stutz, J.L. Reboud, Measurements within unsteady cavitation, Exp. Fluids 29 (2000) 545–552.
[4] B. Stutz, Influence of roughness one the two-phase flow structure of sheet cavitation, J. Fluids Eng. 125 (2003) 652–659.
[5] B. Pouffary, R. Fortes-Patella, J.L. Reboud, Numerical simulation of 3D cavitating flows: Analysis of cavitation head drop in turbomachinery, in: ASME Fluids Engineering Divison Summer Meeting and Exhibition, Houston, USA, June 2005.
[6] B. Pouffary, R. Fortes-Patella, J.L. Reboud, Numerical analysis of cavitation instabilities in inducer blade cascade, in: ASME Fluids Engineering Divison Summer Meeting and Exhibition, Houston, USA, June 2005.
[7] O. Coutier-Delgosha, R. Fortes-Patella, J.L. Reboud, N. Hakimi, C. Hirsch, Numerical simulation of cavitating flow in 2D and 3D inducer geometries, Int. J. Numer. Methods Fluids 48 (2) (2005) 135–167.
[8] K.R. Laberteaux, S.L. Ceccio, Flow in the closure region of closed partial attached cavitation, in: J.M. Michel, H. Kato (Eds.), Proceedings of the Third International Symposium on Cavitation, vol. 1, Grenoble, France, 1998, pp. 197–202.
[9] Q. Le, J.P. Franc, J.M. Michel, Partial cavities: global behavior and mean pressure distribution, ASME J. Fluids Eng. 115 (1993) 243–248.
[10] M. Callenaere, J.P. Franc, J.M. Michel, M. Riondet, The cavitation instability induced by the development of a re-entrant jet, J. Fluid Mech. 444 (2001) 223–256.
[11] H. Kamono, H. Kato, H. Yamaguchi, M. Miyanaga, Simulation of cavity flow by ventilated cavitation on a foil section, ASME, New York, ASME-FED-153, 1993, pp. 183–189.
[12] S.L. Ceccio, C.E. Brennen, Observation of the dynamics and acoustics of travelling bubble cavitation, J. Fluid Mech. 233 (1991) 633–660.
[13] C.O. Iyer, S.L. Ceccio, The influence of developed cavitation on the flow of a turbulent shear layer, Phys. Fluids 14 (October 2002) 10.
[14] M. Dular, R. Bachert, B. Stoffel, B. Sirok, Experimental evaluation of numerical simulation of cavitating flow around hydrofoil, Eur. J. Mech. B/Fluids 24 (2005) 522–538.
[15] B. Stutz, S. Legoupil, R. Woo, Measurements within cloud cavitation by means of X-Ray attenuation device, in: ASME Fluids Engineering Divison Summer Meeting and Exhibition, Montreal, Quebec, Canada, July 14–18, 2002.
[16] W. Hassan, S. Legoupil, S. Barre, C. Rebattet, Dynamic vapor fraction measurement in Ariane 5 inducer by x-rays, in: Proceedings of FEDSM2005, 2005 ASME Fluids Engineering Division Summer Meeting and Exhibition, Houston, TX, USA, June 19–23, 2005.
[17] W. Hassan, S. Legoupil, D. Cambellen, S. Barre, "Dynamic localization of vapor fraction in Ariane 5 inducer by x-rays tomography", in: 2005 IEEE Nuclear Science Symposium and Medical Imaging Conference, Porto-Rico, October 23–29, 2005.
[18] B. Pouffary, R. Fortes-Patella, J.L. Reboud, Numerical simulation of cavitating flow around a 2D hydrofoil: a barotropic approach, in: 5th Int. Symp. on Cavitation, Osaka, Japan, 2003.
[19] Y. Delannoy, J.L. Kueny, Two phase flow approach in unsteady cavitation modeling, Cavitation and Multiphase Flow Forum, ASME-FED 98 (1990) 153–158.
[20] J.-L. Reboud, B. Stutz, O. Coutier, Two-phase flow structure of cavitation: experiment and modeling of unsteady effects, in: 3rd Int. Symp. on Cavitation, Grenoble, France, April 1998.
[21] H. Lohrberg, B. Stoffel, R. Fortes-Patella, O. Coutier-Delgosha, J.L. Reboud, Numerical and experimental investigation on the cavitating flow in a cascade of hydrofoils, Exp. Fluids 33 (4) (2002) 578–586.
[22] O. Coutier-Delgosha, J.L. Reboud, Y. Delannoy, Numerical simulation of the unsteady behavior of cavitating flows, Int. J. Numer. Methods Fluids 42 (5) (2003) 527–548.

[23] O. Coutier-Delgosha, R. Fortes-Patella, J.L. Reboud, Simulation of unsteady cavitation with a two-equations turbulence model including compressibility effects, J. Turbulence 3 (2002) 058, http://jot.iop.org.
[24] R. Fortes Patella, O. Coutier-Delgosha, J. Perrin, J.L. Reboud, A numerical model to predict unsteady cavitating flow behavior in inducer blade cascades, J. Fluids Eng. 129 (2007) 128–135.
[25] O. Coutier-Delgosha, R. Fortes-Patella, J.L. Reboud, N. Hakimi, C. Hirsch, Stability of preconditioned Navier–Stokes equations associated with a cavitation model, Computers & Fluids 34 (3) (March 2005) 319–349.
[26] B. Stutz, Analyse de la structure diphasique et instationnaire de poches de cavitation, Ph. D. Thesis, INPG, CREMHYG Laboratory, 1996.
[27] A. Serisawa, I. Kataoka, M. Michivik, S.H. Park, Turbulence structure of air–water bubbly flow – measuring techniques, Int. J. Multiphase Flow 2 (1975) 221–233.
[28] S.T. Revankar, M. Ishii, Local interfacial area measurement in bubbly flow, Int. J. Heat Mass Transfer 35 (1992) 913–925.
[29] N. Hakimi, Preconditioning methods for time dependent Navier–Stokes equations, Ph.D. Thesis, Vrije Univ., Brussels, 1998.
[30] A. Jameson, W. Schmidt, E. Turkel, Numerical solution of the Euler equations by finite-volume methods using Runge–Kutta time stepping schemes, AIAA Paper 81-1259, June 1981.
[31] E. Turkel, Preconditioning methods for solving the incompressible and low speed compressible equations, J. Comput. Phys. 72 (1987) 277–298.
[32] Z. Yang, T.H. Shih, A k–e model for turbulence and transitional boundary layer, in: R.M.C. So, C.G. Speziale, B.E. Launder (Eds.), Near-Wall Turbulent Flows, Elsevier Science Publishers B.V., 1993, pp. 165–175.
[33] N. Hakimi, C. Hirsch, S. Pierret, Presentation and application of a new extended k–ε model with wall functions, in: ECCOMAS, Barcelona, September 2000.
[34] J. Rolland, S. Barre, E. Goncalves, R. Fortes-Patella, Experiments and modeling of cavitating flows in venturi, Part I: Stable cavitation, in: Sixth International Symposium on Cavitation, CAV2006, Wageningen, The Netherlands, September 2006.
[35] J. Rolland, Modélisation des écoulements cavitants dans les inducteurs de turbopompes : prise en compte des effets thermodynamiques, Ph.D. Thesis of Institut National Polytechnique de Grenoble, February 2008 (in French).
[36] B. Pouffary, Simulation numérique d'écoulements 2d/3d cavitants, stationnaires et instationnaires : analyse spécifique pour les turbomachines, Ph.D. Thesis of Institut National Polytechnique de Grenoble, December 2004 (in French).
[37] D.H. Fruman, B. Reboud, J.-L. Stutz, Estimation of thermal effects in cavitation of thermosensible liquids, Int J. Heat Mass Transfer 42 (1999) 3195–3204.
[38] L. Merle, Etude expérimentale et modéle physique d'un écoulement cavitant avec effet thermodynamique, Ph.D. Thesis of Institut National Polytechnique de Grenoble, 1994 (in French).